Analysis on Influences of Intra-Couplings in a MISO Magnetic Beamforming Wireless Power Transfer System

Kyungtae Kim [1], Han-Joon Kim [2], Dong-Wook Seo [3,*] and Ji-Woong Choi [1,*]

[1] Department of Information and Communication Engineering, Daegu Gyeongbuk Institute of Science and Technology (DGIST), 333 Techno Jungang-daero, Hyeonpung-eup, Dalseong-gun, Daegu 42988, Korea; knight27.kim@dgist.ac.kr

[2] Department of Electrical and Computer Engineering, National University of Singapore (NUS), 21 Lower Kent Ridge Rd, Singapore 119077, Singapore; elekhj@nus.edu.sg

[3] Department of Radio Communication Engineering, Korea Maritime and Ocean University (KMOU), 727 Taejong-ro, Yeongdo-gu, Busan 49112, Korea

* Correspondence: dwseo@kmou.ac.kr (D.-W.S.); jwchoi@dgist.ac.kr (J.-W.C.)

Abstract: Magnetic beamforming techniques can enhance the power transfer efficiency using focused magnetic fields by the multiple transmitters to the receivers. However, the intra-couplings that cause power leakage and phase distortion among the arrayed coils inevitably occur due to the deployment of coils having strong couplings between each other. Here, we analyze the adverse influences of intra-couplings and present the advantages of magnetically independent transmitters for multiple-inputs and single-output (MISO) WPT. The independent coil array can achieve focused magnetic fields by simply adjusting the amplitude of the transmitter voltage source without phase adjustment. The system also can eliminate the reactive power with the independent coil array to efficiently use the supplying power from the source. The analytical studies are verified by numerical and circuit simulation and experiments. Our analysis can be generalized to the MISO-WPT with an arbitrary number of transmitters. It can provide insight into designing and implementing the MISO-WPT applying magnetic beamforming.

Keywords: wireless power transfer (WPT); magnetic beamforming; intra-couplings of transmitter array; magnetically independent transmitter array; non-coupling

1. Introduction

Wireless power transfer (WPT) has attracted much attention from academia and industry: electric vehicle [1–4], biomedical device [5,6], wireless powered communication network (WPCN) [7], and unmanned aerial vehicle (UAV) [8]. Recently, most WPT systems use a magnetic field as a medium for transferring power due to the advantages of simple structure and safety for human exposure. However, the magnetic field-based WPT only provides a narrow charging range of less than a few millimeters. This drawback is caused by a characteristic of a magnetic field whose magnitude sharply attenuates as the field propagates into the air. Studies have been conducted using other media such as radio frequency (RF), ultrasound, and laser to expand the charging range. However, these studies have not been popularized because the safety for human exposure is not sufficiently assured [9].

For this reason, studies for improving magnetic field-based WPT have been carried out: a coupled theory with magnetic resonant coil [10], magnetic relay [11], and an optimally shaped dipole coil [12]. Although the above studies achieved outstanding results, the applicable industries were limited due to the massive size of the coil. Another solution to improve the magnetic field-based WPT's efficiency and charging range is deploying a transmitter array configured as multiple coils [13]. Meanwhile, based on the arrangement of multiple coils, studies have been conducted to optimize this configuration. One of

them is magnetic beamforming inspired by multiple-inputs and multiple-outputs (MIMO) beamforming used in the RF communication field [14]. Magnetic beamforming is a promising technology that achieves the maximum PTE in the multiple-inputs and single-output (MISO) and MIMO-WPT by focusing the magnetic fields from the multiple transmitters to the receiver [15]. This focusing mechanism increases the amount of magnetic field passing through the receiver by constructive interference. Therefore, it induces a larger current in the receiver by Faraday's law, delivering more power to the device. According to the authors of [14], a MISO-WPT with magnetic beamforming (named "MagMIMO" in [14]) achieves a PTE of 87% at a charging distance of 2 cm and a PTE of 11% at a maximum charging distance of 40 cm, whereas other commercial wireless chargers have a PTE of about 8–90% at a maximum charging distance under 2 cm.

However, due to multiple coils configuration for magnetic beamforming, the intra-couplings of transmitter array inevitably occur. This phenomenon is shown in Figure 1 that describes the WPT configurations: (a) SISO-WPT, (b) MISO-WPT, (c) SISO-WPT with field analysis when the transmitter is powered, and (d) MISO-WPT with field analysis when the transmitter 2 is powered. Compared with the SISO-WPT of Figure 1a having only a magnetic coupling k_{TR} between the transmitter and the receiver, the MISO-WPT of Figure 1b has additional intra-couplings k_T in the transmitter array. As shown in Figure 1c, the magnetic field from the transmitter propagating to the receiver induces a voltage and a current at the receiver. However, in the case of the MISO-WPT, the magnetic field is also transferred to the other transmitters, as shown in Figure 1d. For this reason, many studies have been carried out from various perspectives to analyze the effect of the intra-couplings on the WPT: a leakage magnetic field [16], an efficiency attenuation [17], and multiple resonant frequencies [13]. As in the above studies, the adverse effects of the intra-coupling to the WPT have been mainly reported. Various studies have been conducted to reduce or eliminate the intra-coupling. The intra-coupling can be reduced by physical principles using unique structures and materials such as three-dimensional coil array [18], heterogeneous coil array [19], magnetic coupling shield ring [20], high permeability materials [21], and overlapped coil array [22]. Additionally, tuning resonance capacitance can make the transmitter array magnetically independent by compensating the intra-coupling [23].
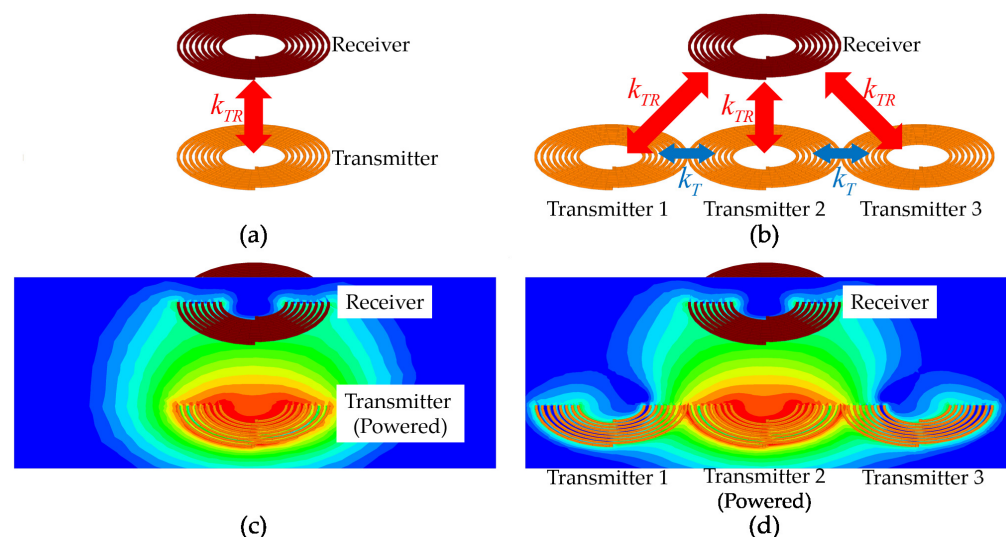
Figure 1. WPT configurations: (**a**) SISO-WPT, (**b**) MISO-WPT, (**c**) SISO-WPT with field analysis, and (**d**) MISO-WPT with field analysis (Transmitter 2 is powered, while other transmitters are power-off).

Most of the studies above provided effective methods to eliminate the intra-couplings. However, the analysis on the intra-coupling from viewpoints of applying magnetic beamforming to MISO-WPT has not yet been analyzed. Accordingly, this paper analyzes the

intra-couplings of transmitter array theoretically and experimentally in terms of magnetic beamforming.

The remainder of the paper is organized as follows. In Section 2, we provide a theoretical background for this work. In Section 3, we provide the theoretical analysis about the intra-couplings of the transmitters: (1) the adverse influences and (2) advantages after elimination. In Section 4, simulation and experiments are performed to verify the theoretical analysis, and the results are provided. The advantages of magnetically independent transmitters in terms of implementation are also derived in Section 4. Conclusions are described in Section 5.

2. Theoretical Backgrounds

2.1. Magnetic Field-Based WPT

Figure 2 shows a typical structure of a magnetic field-based WPT. The alternating current (AC) excites a transmitter coil L_T, causing a time-varying magnetic field into the air. When a portion of the magnetic field penetrates a receiver coil L_R, a magnetic coupling occurs as shown in Figure 1c, which causes the power to be transferred wirelessly. Based on this mechanism, the PTE depends on the magnetic coupling strength between the transmitter and the receiver.

The compensation topologies on both sides make the transmitter and receiver resonate at an identical resonant frequency. This resonance minimizes the power supply's switching losses and volt-ampere (VA) rating [24] and improves the PTE [25,26]. In the receiver, an AC-DC rectifier is inserted to convert AC to direct current (DC). In the remainder of this paper, WPT refers to the magnetic-based WPT shown in Figure 2.
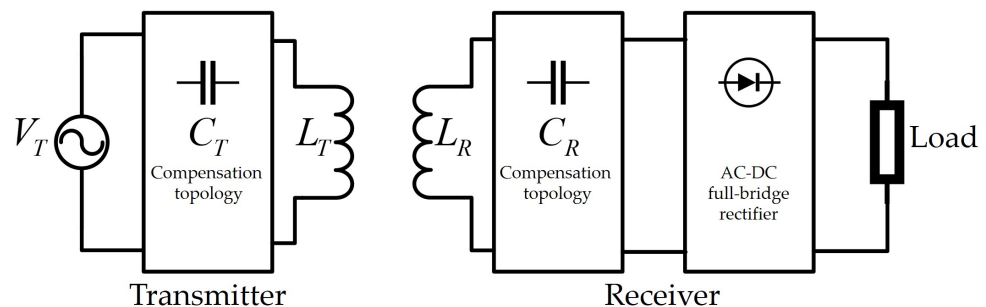
**Figure 2.** Typical structure of magnetic field-based WPT.

2.2. Circuit Modeling for Single-Input and Single-Output (SISO)-WPT

Figure 3 illustrates a circuit modeling of SISO-WPT: (a) a simplified circuit and (b) an equivalent circuit at magnetic resonance. As shown in Figure 3a, the transmitter consists of an inductance L_T, a winding resistance R_T, a resonant capacitance C_T, and a transmitter voltage V_T. The receiver consists of an inductance L_R, a winding resistance R_R, a resonant capacitance C_R, and a load impedance R_L, where R_L includes an AC-DC rectifier and a load in Figure 2. Both sides are magnetically coupled via a mutual inductance M defined as $M = k\sqrt{L_T L_R}$. k is a coupling coefficient between 0 and 1 determined by a relative distance between L_T and L_R. Based on Kirchhoff's voltage law (KVL), two equations describing Figure 3a are obtained:

$$j\omega M I_T = I_R(R_R + j\omega L_R + \frac{1}{j\omega C_R} + R_L), \tag{1}$$

$$V_T = I_T(j\omega L_T + \frac{1}{j\omega C_T} + R_T) - j\omega M I_R, \tag{2}$$

where ω is an angular frequency, and I_T and I_R are a transmitter and receiver current, respectively.
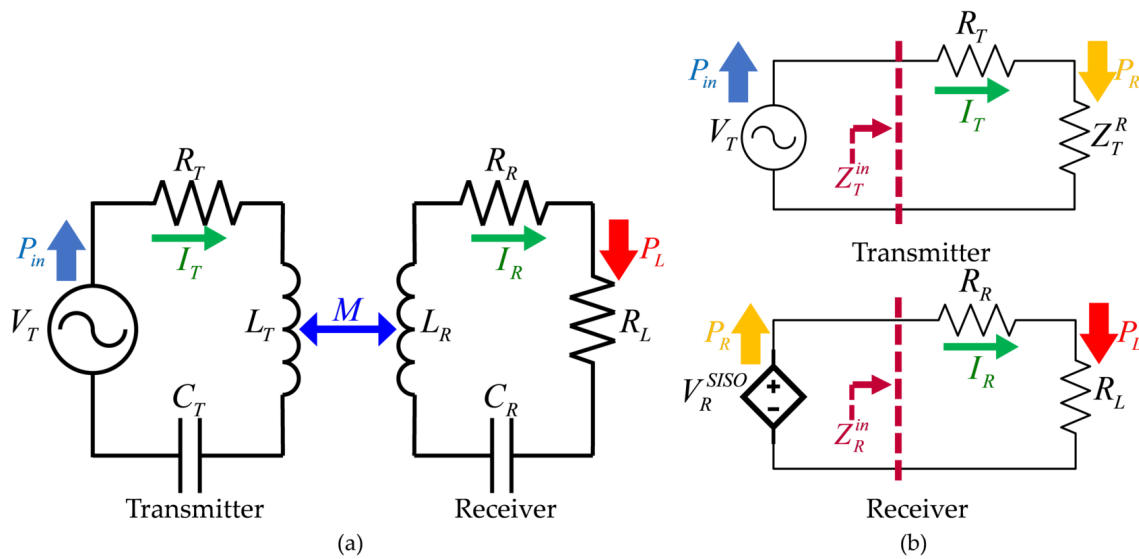
Figure 3. Circuit modeling of SISO-WPT: (**a**) simplified circuit and (**b**) equivalent circuit at magnetic resonance.

Figure 3b illustrates an equivalent circuit of the SISO-WPT at the resonant frequency ω_r that satisfies $\omega_r = 1/\sqrt{L_T C_T} = 1/\sqrt{L_R C_R}$. At ω_r, L and C are eliminated, and the influences on the transmitter and the receiver via the mutual inductance M are as follows: the influence from the transmitter to the receiver is modeled as a current-controlled voltage source V_R^{SISO}, while the influence from the receiver to the transmitter is modeled as a variable reflected impedance Z_T^R. Here, V_R^{SISO} and Z_T^R are given by

$$V_R^{SISO} = j\omega_r M I_T, \tag{3}$$

$$Z_T^R = \frac{(\omega_r M)^2}{Z_R^{in}}, \tag{4}$$

where Z_R^{in} is an input impedance of the receiver seen from V_R^{SISO} (i.e., $Z_R^{in} = R_R + R_L$).

The PTE η_{SISO} is defined as the output power P_L at the load impedance R_L divided by the input power P_{in} supplied from V_T, as shown in Figure 3a (i.e., $\eta_{SISO} = \frac{P_L}{P_{in}}$). η_{SISO} is calculated by an equivalent circuit of Figure 3b. In Figure 3b, the PTE of transmitter and receiver, η_T and η_R, respectively, are given by

$$\eta_T = \frac{P_R}{P_{in}} = \frac{Re(Z_T^R)}{Re(Z_T^{in})} = \frac{Re(Z_T^R)}{R_T + Re(Z_T^R)}, \tag{5}$$

$$\eta_R = \frac{P_L}{P_R} = \frac{R_L}{Re(Z_R^{in})} = \frac{R_L}{R_R + R_L}. \tag{6}$$

Z_T^{in} is the input impedances seen from V_T, as shown in Figure 3b. At the resonant frequency ω_r, Z_T^R is a real value by Equation (4) and therefore Z_T^{in} is also a real value. Accordingly, η_{SISO} at ω_r is calculated as the product of η_T and η_R:

$$\eta_{SISO} = \eta_T \eta_R = \frac{Z_T^R}{R_T + Z_T^R} \frac{R_L}{R_R + R_L}. \tag{7}$$

Equation (7) indicates the correlation between the magnetic coupling strength between the transmitter and receiver and the PTE η_{SISO}. As the charging distance becomes shorter, the magnetic coupling between the two coils stronger, which increases the value of M and Z_T^R. The increased Z_T^R increases η_T, which finally increases η_{SISO}.

2.3. Circuit Modeling of Multiple-Inputs and Single-Output (MISO)-WPT

Figure 4 illustrates a circuit modeling of MISO-WPT configured as N transmitters and a single receiver: (a) a simplified circuit and (b) an equivalent circuit at ω_r. L, R, C, V, I, and P with a subscript Ti indicate the inductance, resistance, capacitance, voltage, current, and power of the i-th transmitter, respectively. Contrary to the SISO-WPT, there are two types of mutual inductances in the MISO-WPT: M_{iR} between L_{Ti} and L_R, and M_{Tiu} $(i \neq u)$ between L_{Ti} and L_{Tu}. k is represented by the identical subscript used for M (i.e., k_{iR} and k_{Tiu}). M_{Tiu} and k_{Tiu} indicate the strength of intra-couplings in the transmitter array. Based on Equations (1) and (2), two equations are derived for describing the MISO-WPT at ω_r as follows:

$$\overrightarrow{\mathbf{V_T}} = \left(\mathbf{Z_T} + \frac{\omega_r^2 \overrightarrow{\mathbf{M}}^T \overrightarrow{\mathbf{M}}}{Z_R^{in}} \right) \overrightarrow{\mathbf{I_T}}, \tag{8}$$

$$I_R = \overrightarrow{\mathbf{H}} \overrightarrow{\mathbf{I_T}} = \frac{j\omega_r \overrightarrow{\mathbf{M}}}{Z_R^{in}} \overrightarrow{\mathbf{I_T}}, \tag{9}$$

where vector and matrix denotations are listed in Table 1.

Figure 4b illustrates an equivalent circuit of the i-th transmitter and receiver of the MISO-WPT at ω_r. In view of each transmitter, the influences from a receiver and other $N-1$ transmitters at ω_r are modeled as a reflected impedance Z_{Ti}^R due to M_{iR} and reflected impedance Z_{Ti}^T due to M_{Tiu}. Here, Z_{Ti}^R and Z_{Ti}^T are expressed as

$$Z_{Ti}^R = \frac{\omega_r^2}{Z_R^{in}} \frac{M_{iR}}{I_{Ti}} \left(\sum_{u=1}^{N} M_{uR} I_{Tu} \right), \tag{10}$$

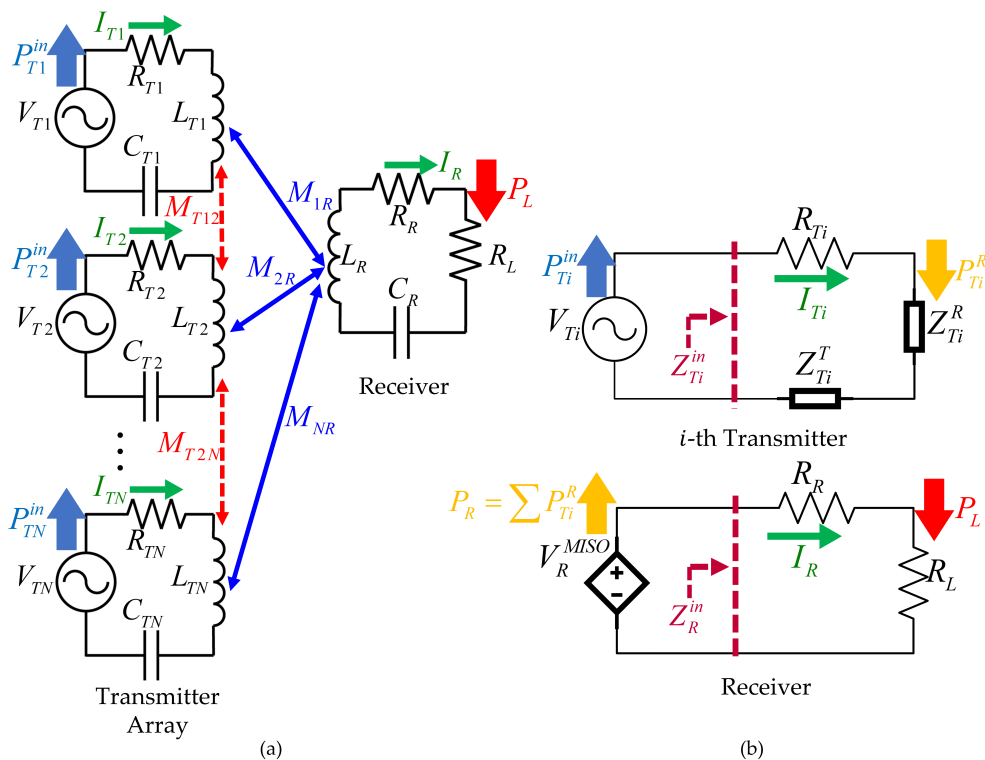$$Z_{Ti}^T = \frac{j\omega_r}{I_{Ti}} \left(\sum_{v=1, v \neq i}^{N} M_{Tiv} I_{Tv} \right). \tag{11}$$

Figure 4. Circuit modeling of MISO-WPT: (**a**) simplified circuit and (**b**) equivalent circuit at magnetic resonance.

Table 1. Vector and matrix denotations for MISO-WPT.
.

Symbol	Definition	Description
N	Number of transmitters	
$\overrightarrow{\mathbf{I_T}}$	$[I_{T1} \ I_{T2} \ \cdots \ I_{TN}]^T$	Set of transmitter current
$\overrightarrow{\mathbf{V_T}}$	$[V_{T1} \ I_{V2} \ \cdots \ V_{TN}]^T$	Set of transmitter voltage
$\mathbf{Z_T}$	$\begin{bmatrix} R_{T1} & j\omega M_{T12} & \cdots & j\omega M_{T1N} \\ j\omega M_{T21} & R_{T2} & \cdots & j\omega M_{T2N} \\ \vdots & \vdots & \ddots & \vdots \\ j\omega M_{TN1} & j\omega M_{TN2} & \cdots & R_{TN} \end{bmatrix}$	Resistance and mutual inductance in transmitter array
$\overrightarrow{\mathbf{M}}$	$[M_{1R} \ M_{2R} \ \cdots \ M_{NR}]$	Mutual inductance between transmitter array and receiver
$\overrightarrow{\mathbf{H}}$	$j\omega_r\overrightarrow{\mathbf{M}}/Z_R^{in}$	Magnetic channel connecting transmitter and receiver current

Based on Equation (3), the current-controlled voltage source V_R^{MISO} at the receiver is expressed as $V_R^{MISO} = j\omega_r\overrightarrow{\mathbf{M}}\overrightarrow{\mathbf{I_T}}$, which implies that all transmitter currents affect V_R^{MISO} through the mutual inductance $\overrightarrow{\mathbf{M}}$.

As shown in Figure 4a, the PTE η_{MISO} is defined as P_L/P_{in}, where P_{in} is sum of supplied power from the voltage source $\overrightarrow{\mathbf{V_T}}$ (i.e., $P_{in} = P_{T1}^{in} + P_{T2}^{in} \cdots + P_{TN}^{in}$). However, calculating η_{MISO} is rather complicated than η_{SISO} of Equation (7). This is because the reflected impedance Z_{Ti}^T and Z_{Ti}^R are complex impedance as both impedances by Equations (10) and (11) are function of the transmitter current with an amplitude and a phase (i.e., $I_{Ti} = |I_{Ti}|\angle I_{Ti}$). Thus, as shown in Figure 4b, the input impedance Z_{Ti}^{in} is a complex impedance, and the *i*-th transmitter's PTE η_{Ti} is given by

$$\eta_{Ti} = \frac{P_{Ti}^R}{P_{Ti}^{in}} = \frac{Re\left(Z_{Ti}^R\right)}{Re\left(Z_{Ti}^{in}\right)} = \frac{Re\left(Z_{Ti}^R\right)}{R_{Ti} + Re\left(Z_{Ti}^T + Z_{Ti}^R\right)}, \tag{12}$$

where P_{Ti}^{in} and P_{Ti}^R are the supplied power from V_{Ti} and the transferred power to the receiver from *i*-th transmitter, respectively. The receiver's PTE η_R is identical to Equation (6).

Different from η_{SISO}, η_{MISO} cannot be directly derived from the efficiency of transmitter and receiver. Therefore, η_{MISO} is calculated by considering the power supplied from $\overrightarrow{\mathbf{V_T}}$. Based on the circuit theory, the phase of impedance Z_{Ti}^{in} causes a phase deviation between V_{Ti} and I_{Ti}, and the power supplied from V_{Ti} is apparent power composed of both active and reactive power [27]. The power transferred and consumed at the load impedance is active power, while the power circulating without being consumed is reactive power. Accordingly, the PTE η_{MISO} is calculated by considering only the active power as follows:

$$\eta_{MISO} = \frac{P_L}{P_{in}} = \frac{|I_R|^2 R_L}{\sum_{i=1}^N Re(V_{Ti}I_{Ti}^*)} = \frac{|I_R|^2 R_L}{\sum_{i=1}^N |I_{Ti}|^2 Re\left(Z_{Ti}^{in}\right)}, \tag{13}$$

where $*$ is a complex conjugate.

2.4. Introduction of Magnetic Beamforming

Magnetic beamforming accomplishes the maximum PTE of the WPT by focusing the magnetic fields from multiple transmitters to the receiver [14,15]. This scheme is applied by adjusting $\overrightarrow{\mathbf{I_T}}$ and $\overrightarrow{\mathbf{V_T}}$ to the beamforming current $\overrightarrow{\mathbf{I_T^{bf}}}$ and voltage $\overrightarrow{\mathbf{V_T^{bf}}}$. $\overrightarrow{\mathbf{I_T^{bf}}}$ and $\overrightarrow{\mathbf{V_T^{bf}}}$ are derived as follows.

The principle is that the active power is distributed only at the resistance, not the capacitance and the inductance. In the MISO-WPT shown in Figure 4a, the total input active power P_{in} supplied from $\overrightarrow{\mathbf{V_T}}$ is distributed at all resistances $\mathbf{R_T}$ and R_R^{in}, where $\mathbf{R_T}$ is $Re(\mathbf{Z_T})$. The active power P_T distributed at all N transmitters is given by $P_T = \overrightarrow{\mathbf{I_T}}^*\mathbf{R_T}\overrightarrow{\mathbf{I_T}}$. The active

power P_R distributed at the receiver is computed as $P_R = I_R{}^2 R_R^{in}$, where $R_R^{in} = Z_R^{in}$. Accordingly, the total input active power P_{in} is the sum of P_T and P_R:

$$P_{in} = P_T + P_R = \overrightarrow{\mathbf{I_T}}^* \mathbf{R_T} \overrightarrow{\mathbf{I_T}} + I_R{}^2 R_R^{in}. \tag{14}$$

Substituting I_R of Equations (9) into (14) yields

$$P_{in} = \overrightarrow{\mathbf{I_T}}^* \mathbf{R_T} \overrightarrow{\mathbf{I_T}} + R_R^{in} \overrightarrow{\mathbf{I_T}}^* \overrightarrow{\mathbf{H}}^* \overrightarrow{\mathbf{H}} \overrightarrow{\mathbf{I_T}}, \tag{15}$$

which implies that P_{in} is a function of $\overrightarrow{\mathbf{I_T}}$.

As explained, the beamforming current $\overrightarrow{\mathbf{I_T^{bf}}}$ maximizes the power transferred to the receiver P_R when P_{in} is fixed. Thus, $\overrightarrow{\mathbf{I_T^{bf}}}$ is given by $\overrightarrow{\mathbf{I_T^{bf}}} = argmax(R_R^{in} \overrightarrow{\mathbf{I_T}}^* \overrightarrow{\mathbf{H}}^* \overrightarrow{\mathbf{H}} \overrightarrow{\mathbf{I_T}})$. $\overrightarrow{\mathbf{I_T^{bf}}}$ is calculated via the optimization method as discussed in [15]:

$$\overrightarrow{\mathbf{I_T^{bf}}} = c\, maxeig\left(\overrightarrow{\mathbf{H}}^* \overrightarrow{\mathbf{H}}\right), \tag{16}$$

where $maxeig(\overrightarrow{\mathbf{H}}^* \overrightarrow{\mathbf{H}})$ is an eigenvector v_{max} of $\overrightarrow{\mathbf{H}}^* \overrightarrow{\mathbf{H}}$ that corresponds to the largest real eigenvalue λ_{max} of $\overrightarrow{\mathbf{H}}^* \overrightarrow{\mathbf{H}}$ (i.e., $(\overrightarrow{\mathbf{H}}^* \overrightarrow{\mathbf{H}})v_{max} = \lambda_{max}v_{max}$), and a constant c is determined by P_{in}. Here, the beamforming voltage $\overrightarrow{\mathbf{V_T^{bf}}}$ is given by substituting $\overrightarrow{\mathbf{I_T^{bf}}}$ into Equation (8). In summary, when $\overrightarrow{\mathbf{V_T}}$ is adjusted to $\overrightarrow{\mathbf{V_T^{bf}}}$, the amplitude and phase of $\overrightarrow{\mathbf{I_T}}$ are adjusted to $\overrightarrow{\mathbf{I_T^{bf}}}$ so that magnetic beamforming is applied to the WPT and the maximum PTE is achieved. Readers interested in the magnetic beamforming are encouraged to refer the papers of [14,15].

3. Theoretical Analysis on Influences of Intra-Couplings

In Section 3, we theoretically analyze the influences caused by the intra-couplings of MISO-WPT from viewpoints of magnetic beamforming. Through the analysis, we derive the advantages of magnetically independent transmitters (i.e., M_{Tiu} and k_{Tiu}=0). For theoretical analysis, we first express $\overrightarrow{\mathbf{I_T^{bf}}}$ and $\overrightarrow{\mathbf{V_T^{bf}}}$ as a function of M_{iR} and M_{Tiu}. According to Equation (16), $\overrightarrow{\mathbf{I_T^{bf}}}$ of the MISO-WPT is obtained by v_{max} and λ_{max} of $\overrightarrow{\mathbf{H}}^* \overrightarrow{\mathbf{H}}$. According to Equations (A8) and (A10) in Appendix A, we derive that λ_{max} and v_{max} of $\overrightarrow{\mathbf{H}}^* \overrightarrow{\mathbf{H}}$ are

$$\lambda_{max} = \sum_{i=1}^{N} H_{iR}{}^2 = \sum_{i=1}^{N} \left(\frac{\omega M_{iR}}{R_R^{in}}\right)^2, \tag{17}$$

$$v_{max} = d\, \overrightarrow{\mathbf{M}}^T, \tag{18}$$

where H_{iR} is a magnetic channel between the *i*-th transmitter and receiver, and d is a constant for normalizing v_{max} to a unit vector. By substituting v_{max} of Equation (18) into (16), we obtain

$$\overrightarrow{\mathbf{I_T^{bf}}} = c'\, \overrightarrow{\mathbf{M}}^T, \tag{19}$$

where a constant c' is computed as $c' = cd$, which is determined by P_{in}.

Equation (19) directly provides information on the amplitude and phase of $\overrightarrow{\mathbf{I_T^{bf}}}$, denoted as $|I_{Ti}^{bf}|$ and $\angle \overrightarrow{\mathbf{I_T^{bf}}}$. The amplitude of each transmitter current is proportional to the mutual inductance between each transmitter and receiver (i.e., $I_{Ti}^{bf} \propto M_{Ti}$). All transmitter currents are in phase due to a positive value of the mutual inductance $\overrightarrow{\mathbf{M}}$. By substituting $\overrightarrow{\mathbf{I_T^{bf}}}$ of Equation (19) into Equation (8), we obtain

$$\overrightarrow{\mathbf{V_T^{bf}}} = c' \begin{bmatrix} M_{1R}\left(R_{T1} + \frac{\omega_r^2}{R_R^{in}}\sum_{h=1}^{N} M_{hR}{}^2 + j\omega_r \sum_{u=1, u \neq 1}^{N} M_{T1u}\right) \\ M_{2R}\left(R_{T2} + \frac{\omega_r^2}{R_R^{in}}\sum_{h=1}^{N} M_{hR}{}^2 + j\omega_r \sum_{u=1, u \neq 2}^{N} M_{T2u}\right) \\ \vdots \\ M_{NR}\left(R_{TN} + \frac{\omega_r^2}{R_R^{in}}\sum_{h=1}^{N} M_{hR}{}^2 + j\omega_r \sum_{u=1, u \neq N}^{N} M_{TNu}\right) \end{bmatrix}. \tag{20}$$

From now on, the influences caused by the intra-couplings are theoretically analyzed based on derived $\overrightarrow{\mathbf{I_T^{bf}}}$ and $\overrightarrow{\mathbf{V_T^{bf}}}$ by Equations (19) and (20).

3.1. Influences on Beamforming Voltage

The first influence is that the amplitude and phase of $\overrightarrow{\mathbf{V_T^{bf}}}$, denoted as $|\overrightarrow{\mathbf{V_T^{bf}}}|$ and $\angle\overrightarrow{\mathbf{V_T^{bf}}}$, correspondingly increase as the strength of intra-couplings increases. It is verified by analyzing $\overrightarrow{\mathbf{V_T^{bf}}}$ of Equation (20). According to Equation (19), $\overrightarrow{\mathbf{I_T^{bf}}}$ is determined as a function of P_{in} and $\overrightarrow{\mathbf{M}}$, regardless of M_{Tiu}. This implies that $\overrightarrow{\mathbf{I_T^{bf}}}$ is fixed once the deployment of transmitter/receiver and P_{in} is determined. On the other hand, an imaginary part of $\overrightarrow{\mathbf{V_T^{bf}}}$ of Equation (20) is a function of M_{Tiu} (i.e., $Im(V_{Ti}^{bf}) = c'(j\omega_r \sum_{u=1, u \neq i}^{N} M_{Tiu})$). This implies that $|\overrightarrow{\mathbf{V_T^{bf}}}|$ and $\angle\overrightarrow{\mathbf{V_T^{bf}}}$ increase as M_{Tiu} increases, even though fixed P_{in} and $\overrightarrow{\mathbf{I_T^{bf}}}$ are supplied. For this reason, each transmitter should deploy both the voltage amplifier and phase shifter with a wider control range as M_{Tiu} increases. This requirement complicates the design of the transmitter, which may increase overall costs for the magnetic beamforming WPT system.

Conversely, $|\overrightarrow{\mathbf{V_T^{bf}}}|$ and $\angle\overrightarrow{\mathbf{V_T^{bf}}}$ reduce as M_{Tiu} decreases. If the transmitters become magnetically independent (i.e., the intra-couplings are completely eliminated, $M_{Tiu} = 0$), $|\overrightarrow{\mathbf{V_T^{bf}}}|$ becomes independent of M_{Tiu}, and $\angle\overrightarrow{\mathbf{V_T^{bf}}}$ becomes zero. This is derived by eliminating M_{Tiu} in Equation (20) as follows:

$$\overrightarrow{\mathbf{V_T^{bf}}} = c' \begin{bmatrix} M_{1R}\left(R_{T1} + \frac{\omega_r^2}{R_R^{in}}\sum_{h=1}^{N} M_{hR}{}^2\right) \\ M_{2R}\left(R_{T2} + \frac{\omega_r^2}{R_R^{in}}\sum_{h=1}^{N} M_{hR}{}^2\right) \\ \vdots \\ M_{NR}\left(R_{TN} + \frac{\omega_r^2}{R_R^{in}}\sum_{h=1}^{N} M_{hR}{}^2\right) \end{bmatrix}. \tag{21}$$

Equation (21) indicates that magnetic beamforming is achieved by adjusting only the amplitude of the transmitter voltage when the transmitters are magnetically independent. In other words, the control variables for magnetic beamforming are reduced from two to one. For this reason, it is not necessary to deploy the complicated phase shifter in each transmitter, which makes the design of the transmitter much simpler. This is the first advantage of magnetically independent transmitters when applying magnetic beamforming to the WPT.

Furthermore, $\overrightarrow{\mathbf{V_T^{bf}}}$ of Equation (21) becomes much simplified under an additional condition that all transmitters have identical winding resistance (i.e., $R_T = R_{T1} = R_{T2} \cdots = R_{TN}$). This is a reasonable assumption if the transmitter array is composed of an identical coil. In this case, the simplified $\overrightarrow{\mathbf{V_T^{bf}}}$ is given by

$$\overrightarrow{\mathbf{V_T^{bf}}} = c'' \overrightarrow{\mathbf{M}}^T, \tag{22}$$

where a constant c'' is calculated by $c'' = c'/(R_T + \omega_r^2 \sum_{h=1}^N M_{hR}^2/R_R^{in})$. By comparing Equations (20) and (22), $\overrightarrow{\mathbf{V_T^{bf}}}$ becomes much simpler when the MISO-WPT satisfies the conditions that $M_{Tiu} = 0$ and $R_T = R_{T1} = R_{T2}\cdots = R_{TN}$. That is, in this case, the MISO-WPT achieves magnetic beamforming by only estimating the mutual inductance $\overrightarrow{\mathbf{M}}$ and adjusting the amplitude of transmitter voltage $|\overrightarrow{\mathbf{V_T^{bf}}}|$ without adjusting the angle of transmitter voltage $\angle\overrightarrow{\mathbf{V_T^{bf}}}$. This becomes a significant advantage in designing an adaptive real-time MISO-WPT system with magnetic beamforming.

3.2. Influences on Power Factor

The second influence is that the power factor decreases as the intra-couplings of transmitter array increase when magnetic beamforming is applied. To explain this phenomenon, understanding the concept of "a complex power" described by "a power triangle" is necessary. Figure 5a is a power triangle describing the complex power **S**, the active power P, the reactive power Q, and the power factor angle θ, respectively. P is the actual power dissipated by the resistive load, while Q is a measure of the energy exchange between the source and the reactive part of the load [27,28]. The relationship between **S**, P, and Q is $\mathbf{S} = P + jQ$, and the apparent power S is the absolute value of **S** (i.e., $S = |\mathbf{S}|$).
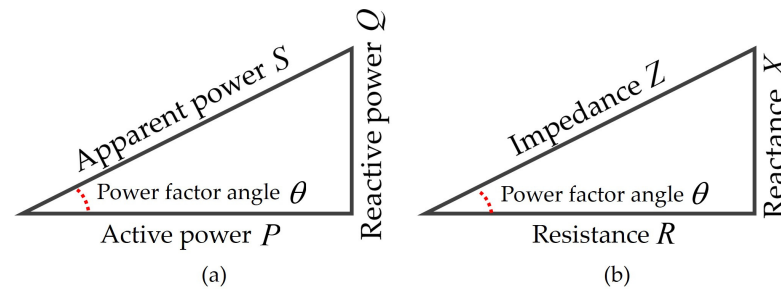

Figure 5. Figures for describing complex power: (**a**) power triangle and (**b**) impedance triangle.

The power factor PF is calculated by the ratio of P to the S (i.e., $PF = P/S = \cos\theta$), and it is important in the AC power system as a measure of how efficiently power is being used [28]. The power triangle is similar to the impedance triangle, shown in Figure 5b, describing the relationship between the impedance Z, the resistance R, and the reactance X, respectively [27]. Both power and impedance have relationships: S, P, and Q are related to Z, R, and X, respectively. From now on, a subscript Ti appended to PF, S, P, Q, and θ indicate the parameter of the i-th transmitter of MISO-WPT.

The influence of M_{Tiu} on PF is derived as follows. By substituting $\overrightarrow{\mathbf{I_T^{bf}}}$ of Equation (19) into Equations (10) and (11), Z_{Ti}^R and Z_{Ti}^T are given by

$$Z_{Ti}^R = \frac{\omega_r^2}{R_R^{in}}\left(\sum_{u=1}^N M_{uR}^2\right), \tag{23}$$

$$Z_{Ti}^T = \frac{j\omega_r}{M_{iR}}\left(\sum_{u=1,u\neq i}^N M_{Tiu}M_{uR}\right). \tag{24}$$

Equations (23) and (24) indicate that Z_{Ti}^R and Z_{Ti}^T become resistive and reactive load, respectively, as M_{uR} and M_{Tiu} are positive real values. That is, the input impedance of i-th transmitter Z_{Ti}^{in} consists of two serially connected resistive load R_{Ti} and Z_{Ti}^R, and one reactive load Z_{Ti}^T (i.e., $Re(Z_{Ti}^{in}) = R_{Ti} + Z_{Ti}^R$ and $Im(Z_{Ti}^{in}) = Z_{Ti}^T$). Here, based on Figure 5b, the power factor of i-th transmitter PF_{Ti} is given by

$$PF_{Ti} = \cos\theta_{Ti} = \cos\left[\tan^{-1}\left(\frac{Im(Z_{Ti}^{in})}{Re(Z_{Ti}^{in})}\right)\right] = \cos\left[\tan^{-1}\left(\frac{Z_{Ti}^T}{R_{Ti} + Z_{Ti}^R}\right)\right]. \tag{25}$$

Equation (25) indicates that θ_{Ti} approaches 90 degrees as Z_{Ti}^T increases, which attenuates PF_{Ti}. That is, as shown in Figure 5b, an increase in M_{Tiu} increases Z_{Ti}^T, which causes θ_{Ti} to increase. An increase in θ_{Ti} increases the reactive power Q_{Ti} and the apparent power S_{Ti}, which causes attenuation of the power factor PF_{Ti}, as shown in Figure 5a.

For this reason, much apparent input power S_{in} ($S_{in} = S_{in}^{T1} + S_{in}^{T2} + \cdots + S_{in}^{TN}$) is required as M_{Tiu} increases when the magnetic beamforming is applied with the fixed P_{in}. Alternatively, when S_{in} is fixed, less P_{in} is supplied from the power supply as M_{Tiu} increases. If the required S_{in} exceeds the VA ratings, which is the maximum apparent power available by power supply, the system operation may become unstable because of an insufficient supply of reactive power [28].

Based on the above explanation, the second advantage of the magnetically independent transmitter is derived. A unity PF_{Ti} is achieved as Z_{Ti}^T and Q_{Ti} are eliminated when the transmitters are magnetically independent. In this case, the apparent power supplied from the voltage source is identical to the active power (i.e., $S_{in} = P_{in}$). According to the work in [28], a high power factor is desirable in AC power systems to improve stability and efficiency and reduce costs. For this reason, it is necessary to reduce the intra-couplings of transmitter array when designing the MISO-WPT with magnetic beamforming. This advantage is essential in fields where a stable high power supply is required, such as electric vehicle charging.

3.3. Influences on Power Transfer Efficiency

It is expected that the intra-couplings M_{Tiu} affect the PTE η_{MISO} since η_{Ti} has Z_{Ti}^T in the denominator of Equation (12) which is a function of M_{Tiu}. However, in conclusion, the PTE η_{MISO} is determined regardless of M_{Tiu} under magnetic beamforming status. The reason is that the in-phase characteristic of beamforming current $\overrightarrow{\mathbf{I_T^{bf}}}$ makes the reflected impedance Z_{Ti}^T a reactive load, as expressed in Equation (24). Therefore, η_{Ti} under magnetic beamforming status is given by

$$\eta_{Ti} = \frac{P_{Ti}^R}{P_{Ti}^{in}} = \frac{Re\left(Z_{Ti}^R\right)}{Re\left(Z_{Ti}^{in}\right)} = \frac{Z_{Ti}^R}{R_{Ti} + Z_{Ti}^R}. \tag{26}$$

Based on Equation (23), the reflected impedance Z_{Ti}^R at each transmitter is identical when magnetic beamforming is applied (i.e., $Z_T^R = Z_{T1}^R = Z_{T2}^R \cdots = Z_{TN}^R$), which makes the PTE of each transmitter is identical (i.e., $\eta_T = \eta_{T1} = \eta_{T2} \cdots = \eta_{TN}$). For this reason, when all winding resistance of transmitter is identical, the PTE η_{MISO} under magnetic beamforming status is given by

$$\eta_{MISO} = \frac{P_L}{P_{in}} = \eta_T \eta_R = \frac{Z_T^R}{R_T + Z_T^R} \frac{R_L}{R_R + R_L}. \tag{27}$$

In summary, Equation (27) implies that η_{MISO} under magnetic beamforming can be simply calculated by multiplying the efficiency of any transmitter and receiver, and η_{MISO} is determined regardless of the intra-couplings of transmitter array.

4. Verification via Simulation and Experiment

Thus far, the influences of the intra-couplings of transmitter array and the advantages of magnetically independent transmitters have been analyzed theoretically. In this section, MATLAB/SPICE simulation and experiment are carried out, and the results are analyzed and compared. Based on the results, we verify the superiority of magnetically independent transmitters from various viewpoints. The MISO-WPT with two transmitters and one receiver is adopted for the simulation and experiment.

4.1. Simulation and Experiment Setting

Figure 6 describes the circuit designs of transmitter and receiver for the simulation and experiment. The requirements of the transmitter used for magnetic beamforming are as follows: (1) it can easily adjust the amplitude and phase of the transmitter voltage, and (2) it can flow a large current. As shown in Figure 6a,b, we adopt a class-D amplifier satisfying the above requirements as the transmitter, and we deploy an AC-DC full-bridge rectifier in the receiver to convert AC to DC.
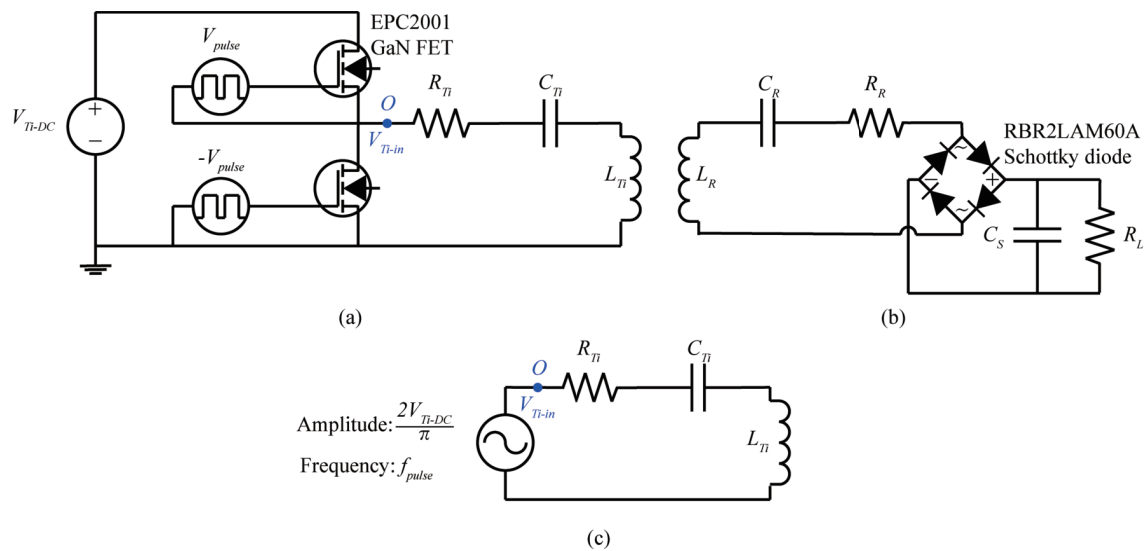
Figure 6. Circuit design for simulation and experiment: (**a**) class-D amplifier for transmitter, (**b**) receiver with full-bridge rectifier and smoothing capacitor, and (**c**) equivalent transmitter circuit of Figure 6a.

Our designed WPT system operates as follows. As shown in Figure 6a, the class-D amplifier composed of two field-effect transistors (FETs) operates as a voltage source where the output is a square wave voltage. The two FETs are turned on and off complementarily with a duty ratio of 50% by an inverter and a square wave voltage V_{pulse}. The amplitude of V_{pulse} should be higher than a gate-source threshold voltage of the FET to function the FET as a switch. The frequency f_{pulse} of V_{pulse} is chosen identical to the resonant frequency f_r determined by L_{Ti} and C_{Ti}. A DC voltage source V_{Ti-DC} connected at a drain of upper FET is a DC power supply to flow the transmitter current. After applying V_{Ti-DC} and V_{pulse}, a square wave output voltage V_{Ti-in} where the amplitude and the frequency are V_{Ti-DC} and f_{pulse} is generated at point O of Figure 6a. Next, the generated V_{Ti-in} passes through a series LC filter composed of L_{Ti} and C_{Ti}. As f_{pulse} is identical as f_r, a sine wave having the amplitude is $2V_{Ti-DC}/\pi$ and the frequency is f_{pulse}, a first harmonic of V_{Ti-in}, passes through the LC filter. Figure 6c is an equivalent circuit of class-D amplifier explained above. On the receiver side shown in Figure 6b, an AC-DC full-bridge rectifier and a smoothing capacitance C_S are deployed to supply DC to the load impedance R_L. Figure 7 shows implemented circuits of transmitter and receiver based on Figure 6.

The elements used for the simulation and experiment are as follows. As a switch in the class-D amplifier, an EPC2001 FET of Efficient Power Conversion (EPC) is used. This FET made of gallium nitride (GaN) can flow a large current and operate at the high-frequency [29]. The full-bridge AC-DC rectifier is composed of RBR2LAM60A, a Schottky diode of ROHM. This diode provides better efficiency due to its lower forward voltage drop of 0.65 V and fast-recovery characteristic. The inductance L_{Ti} and L_R are manufactured using hollow copper tubes in a spiral shape. The outer and inner diameter of L_{Ti} and L_R is 27.5 cm and 17.5 cm. The self-inductance value is 7.4 µH, which is measured by the network analyzer E5061B of Keysight.

For the experiment, we choose the overlapping method among the methods introduced in Section 1 to adjust the strength of intra-couplings. This is because the overlapping

method can easily adjust the strength of intra-couplings without affecting other parameters and realizes without additional active devices and power supplies [22]. Figure 8 shows an adjustment of coupling coefficient k_{T12} between transmitters by the overlapping method. It is verified by the network analyzer that k_{T12} is adjusted from 0 to 0.06 (M_{T12} is adjusted from 0 to 0.44 µH). Figure 9 shows the transmitter array and receiver deployed for the experiment. The parameter values are listed in Table 2.

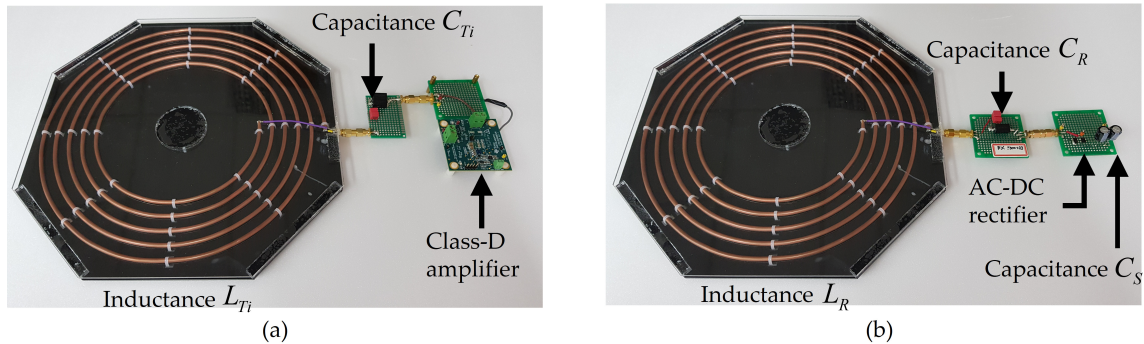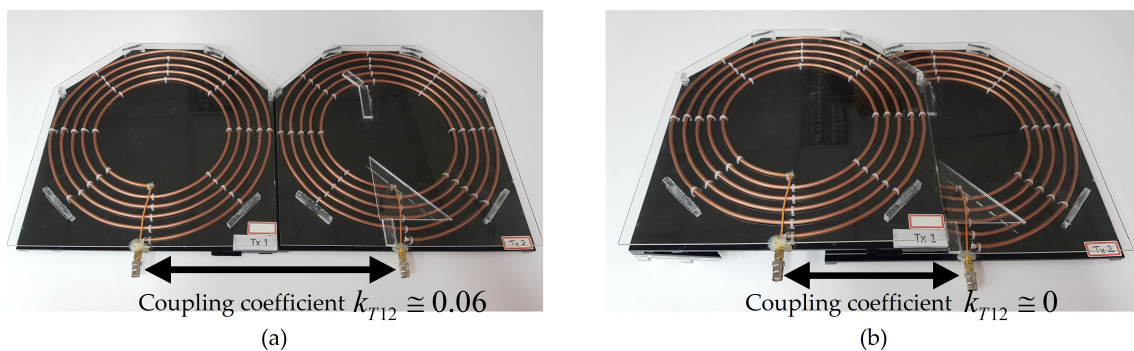**Figure 7.** Implementation based on Figure 6: (**a**) transmitter and (**b**) receiver.

Figure 8. Adjustment of k_{T12} by overlapping method: (**a**) $k_{T12} = 0.06$ and (**b**) $k_{T12} = 0$.
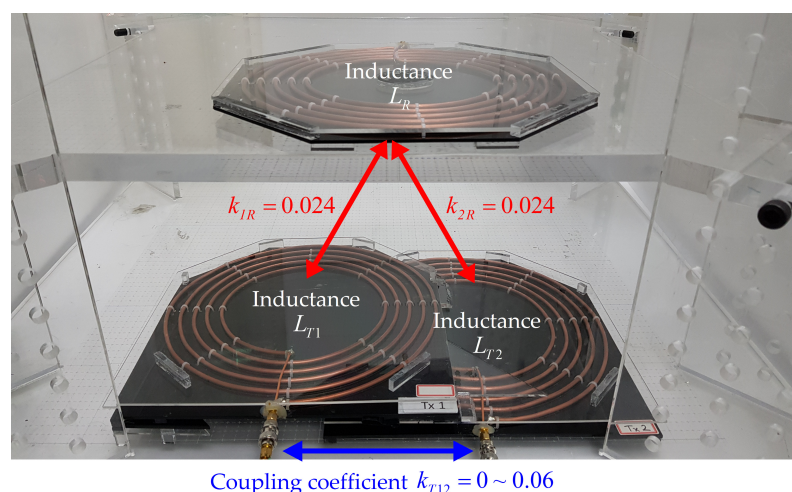

Figure 9. Deployment of transmitter array and receiver.

4.2. Simulation and Experiment Results

MATLAB simulation is carried out based on the equations in Sections 2 and 3 using the parameters in Table 2. It provides the theoretical analysis of the designed MISO-WPT with magnetic beamforming. The SPICE simulation and experiment are carried out based on the circuits shown in Figures 6 and 7. Both simulation and experiment are carried out

under two conditions where the input active power P_{in} and input apparent power S_{in} (i.e., $P_{in} = P_{in}^{T1} + P_{in}^{T2}$ and $S_{in} = S_{in}^{T1} + S_{in}^{T2}$) are fixed at specific values.

Table 2. Parameters for the simulation and experiment.

Symbol	Value	Description
R_{Ti}, R_R	1 Ω	Winding resistance of inductance L_{Ti}, L_R
R_L	5 Ω	Load impedance indicating the device to be charged
C_{Ti}, C_R	3.4 nF	Capacitance for resonance at 1 MHz
L_{Ti}, L_R	7.4 μH	Inductance of transmitter and receiver
C_S	13.2 μF	Smoothing capacitance in receiver
f_r	1 MHz	Resonant frequency
k_{1R}, k_{2R}	0.024	Coupling coefficient between each transmitter and receiver
M_{1R}, M_{2R}	0.178 μH	Mutual inductance between each transmitter and receiver
k_{T12}	0∼0.06	Coupling coefficient in transmitter array
M_{T12}	0∼0.44 μH	Mutual inductance in transmitter array

4.2.1. Fixed P_{in} at 5 W

The condition of fixed input active power P_{in} indicates that the power supply always supplies the constant P_{in} regardless of the input apparent power S_{in} and the input reactive power Q_{in}. For the simple analysis, we set P_{in} at 5 W. Figure 10 plots $\overrightarrow{\mathbf{V_T^{bf}}}$ calculated by Equation (20) with parameters in Table 2 and 5 W P_{in}: (a) the amplitude $|V_{Ti}^{bf}|$ and (b) the phase $\angle V_{Ti}^{bf}$. As shown in Figure 9, the magnetic coupling strength between each transmitter and receiver is identical (i.e., $k_{1R} = k_{2R}$, $M_{1R} = M_{2R}$) due to its symmetrical deployment. For this reason, each transmitter has an identical beamforming current and voltage (i.e., $V_{T1}^{bf} = V_{T2}^{bf}$ and $I_{T1}^{bf} = I_{T2}^{bf}$). As shown in Figure 10, $|V_{Ti}^{bf}|$ and $\angle V_{Ti}^{bf}$ increase as k_{T12} increases. $\angle V_{Ti}^{bf}$ is 0 degrees when the transmitters are magnetically independent, which implies that the phase adjustment is unnecessary in this case. The results in Figure 10 are used as input variables for the voltage source of the simulation and experiment.
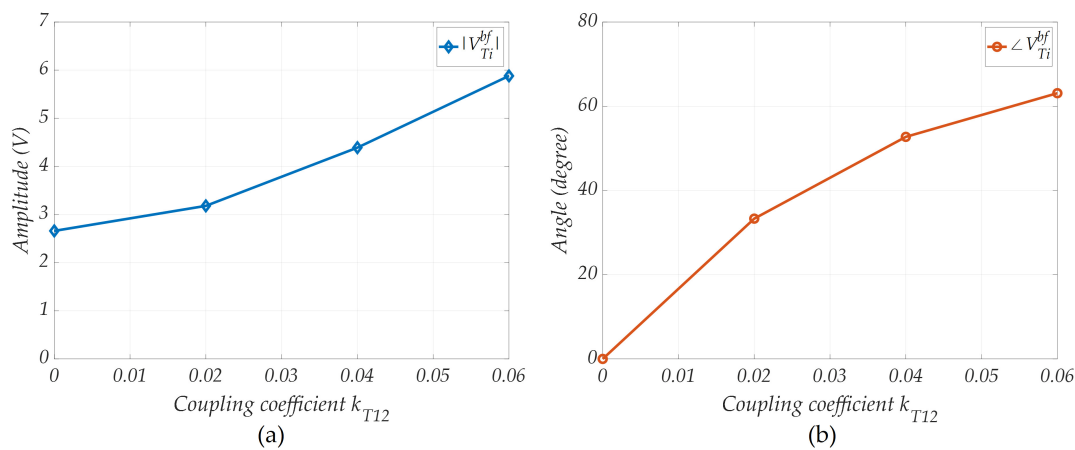
Figure 10. $\overrightarrow{\mathbf{V_T^{bf}}}$ when P_{in} is fixed at 5 W: (**a**) $|V_{Ti}^{bf}|$ and (**b**) $\angle V_{Ti}^{bf}$.

Figure 11 plots $\overrightarrow{\mathbf{I_T^{bf}}}$ and I_R after applying $\overrightarrow{\mathbf{V_T^{bf}}}$: (a) $|I_{Ti}^{bf}|$ and (b) $|I_R|$. MATLAB results are plotted using Equations (9) and (19). As shown in Figure 11, MATLAB results of $|I_{Ti}^{bf}|$ and $|I_R|$ are constant at about 1.9 A and 0.7 A, even though $|V_{Ti}^{bf}|$ increases as k_{T12} increases. This is because $\overrightarrow{\mathbf{I_T^{bf}}}$ is determined regardless of k_{T12} according to Equation (19). SPICE and experimental results also plot identical tendencies. Note that although the experimental results of I_{T1}^{bf} and I_{T2}^{bf} are different due to measurement error, product tolerance, and

parasitic components of elements, the difference is negligible. Based on the above results, it is verified that k_{T12} inhibits the increase in $\overrightarrow{\mathbf{I_T^{bf}}}$ even if $\overrightarrow{\mathbf{V_T^{bf}}}$ increases.

Figure 12 plots the results after applying $\overrightarrow{\mathbf{V_T^{bf}}}$: (a) the input active power P_{in}, (b) the power to the load P_L, and (c) the PTE η_{MISO}. MATLAB results of P_L and η_{MISO}, calculated using Equation (13), are constant at 1.2 W P_L and 24% η_{MISO} regardless of k_{T12}. These results are theoretical maximum values as magnetic beamforming achieves the maximum PTE, as explained in Section 2.4. SPICE and experimental results plot identical tendencies, although there are slight attenuations of about 0.4 W P_L and 9% PTE compared to MATLAB results. These attenuations are caused by parasitic components of elements used in SPICE and experiment, such as the forward voltage drop of a diode and turn-on resistance of a FET.

Based on the above results, $\overrightarrow{\mathbf{I_T^{bf}}}$ and η_{MISO} remain constant even if $\overrightarrow{\mathbf{V_T^{bf}}}$ increases as k_{T12} increases. The result of the increased voltage is verified by apparent power, reactive power, and power factor. Figure 13 plots the results after applying $\overrightarrow{\mathbf{V_T^{bf}}}$: (a) the input apparent power S_{in}, (b) the input reactive power Q_{in}, and (c) the power factor PF_{in}. S_{in} and Q_{in} are the sums of apparent and reactive power from V_{T1-DC} and V_{T2-DC}, and PF_{in} is given by $PF_{in} = P_{in}/S_{in}$. MATLAB results of PF_{in} are plotted by Equation (25). As shown in Figure 13a,b, S_{in} and Q_{in} increase as k_{T12} increases. When k_{T12} is 0.06, approximately 11 VA S_{in} and 10 VAR Q_{in} should be supplied even if 5 W P_{in} is constantly supplied from the power supply. These results indicate that the reactive power, not contributing to the active power, linearly increases as k_{T12} increases, thereby increasing the apparent power required from the power supply. For this reason, PF_{in} shown in Figure 13c sharply drops under 0.5 when k_{T12} is 0.06.
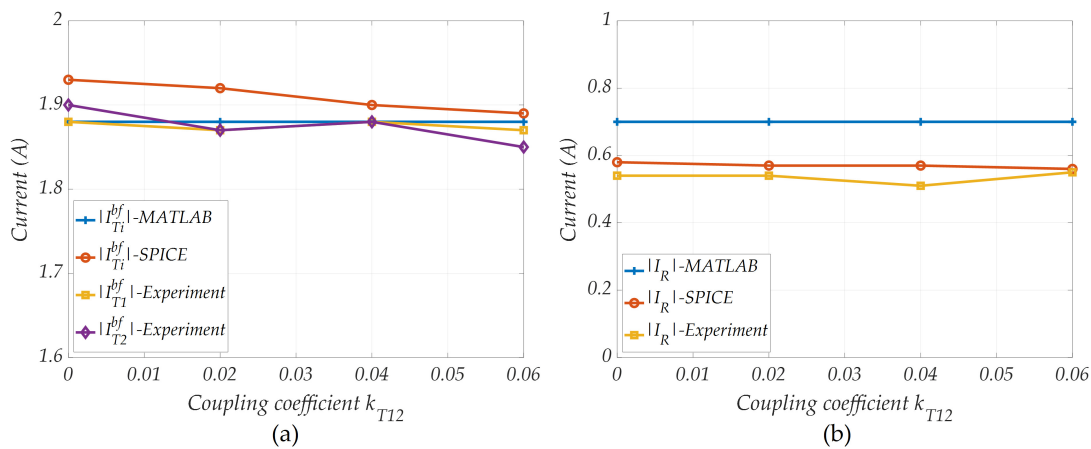

Figure 11. Currents after applying $\overrightarrow{\mathbf{V_T^{bf}}}$: (**a**) $|I_{Ti}^{bf}|$ and (**b**) $|I_R|$.
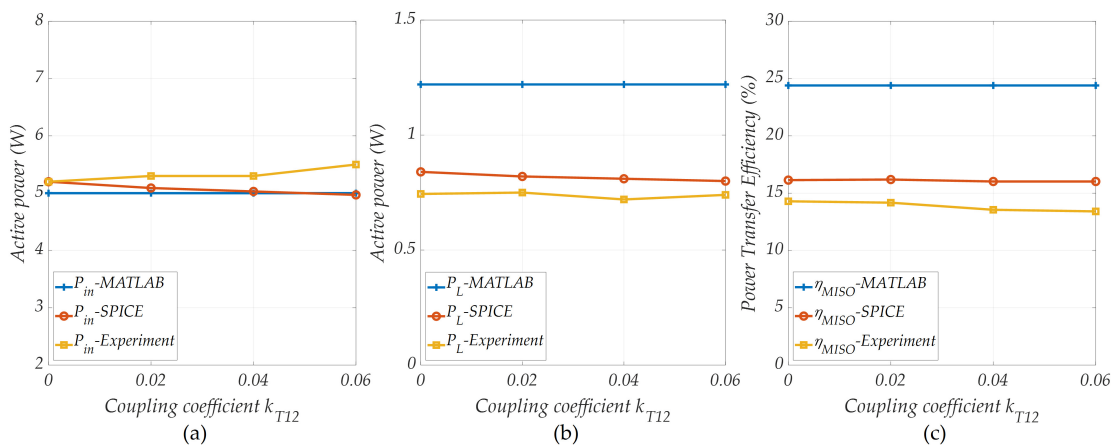
Figure 12. Results after applying $\overrightarrow{\mathbf{V_T^{bf}}}$: (**a**) P_{in}, (**b**) P_L, and (**c**) η_{MISO}.
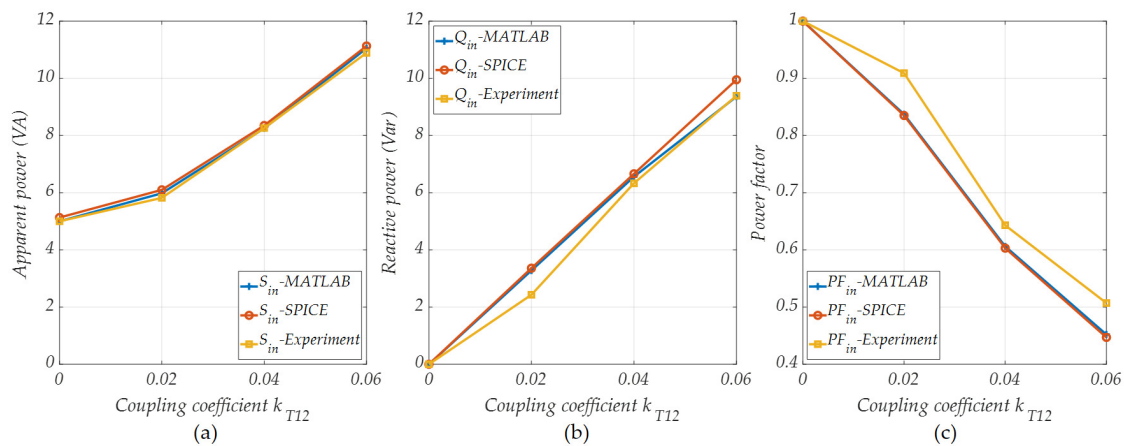
Figure 13. Results after applying $\overrightarrow{\mathbf{V_T^{bf}}}$: (**a**) S_{in}, (**b**) Q_{in}, and (**c**) PF_{in}.

4.2.2. Fixed S_{in} at 5 VA

The previous simulation and experiment are carried out under the assumption that the power supply can supply an unlimited amount of apparent power. However, there is an upper limit on the maximum apparent power that the power supply can provide in practice called the VA rating. It is a unit concept mainly applied to electrical equipment such as a transformer, a power supply, and an uninterruptible power supply (UPS). Therefore, it is meaningful to analyze the influences of intra-couplings when the power supply operates maximally at the VA rating. For simplicity, we set the VA rating of the power supply as 5 VA, and the system operates at this VA rating (i.e., S_{in} = 5 VA).

Figure 14 plots $\overrightarrow{\mathbf{V_T^{bf}}}$ by Equation (20) when S_{in} is fixed at 5 VA: (a) the amplitude $|V_{Ti}^{bf}|$ and (b) the phase $\angle V_{Ti}^{bf}$. Same as before, the results in Figure 14 are used as input variables for the voltage source of the simulation and experiment. By comparing Figures 10 and 14, $\angle\overrightarrow{\mathbf{V_T^{bf}}}$ of both results are identical. This is because the constant c' related to P_{in} in Equation (20) is eliminated during the calculation for $\angle\overrightarrow{\mathbf{V_T^{bf}}}$. On the other hand, $|V_{Ti}^{bf}|$ is varied by depending on whether the fixed P_{in} or S_{in}. The following graphs are the results when the $\overrightarrow{\mathbf{V_T^{bf}}}$ of Figure 14 is applied. Figure 15 plots the amplitude of currents: (a) $|I_{Ti}^{bf}|$ and (b) $|I_R|$. Figure 16 plots the results after applying $\overrightarrow{\mathbf{V_T^{bf}}}$ of Figure 14: (a) the input active power P_{in}, (b) the power dissipated to the load P_L, and (c) the PTE η_{MISO}. Figure 17 plots the results: (a) the input apparent power S_{in}, (b) the input reactive power Q_{in}, and (c) the power factor PF_{in}.
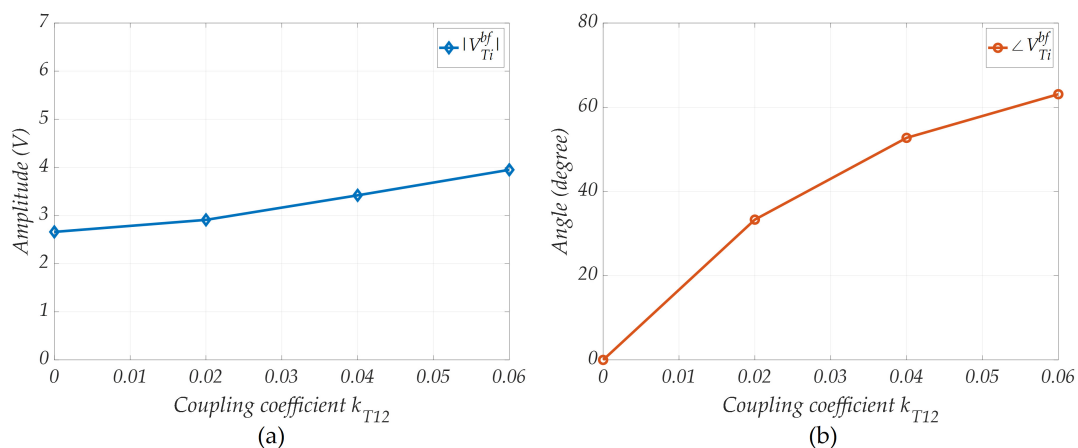

Figure 14. $\overrightarrow{\mathbf{V_T^{bf}}}$ when S_{in} is fixed at 5 VA: (**a**) $|V_{Ti}^{bf}|$ and (**b**) $\angle V_{Ti}^{bf}$.
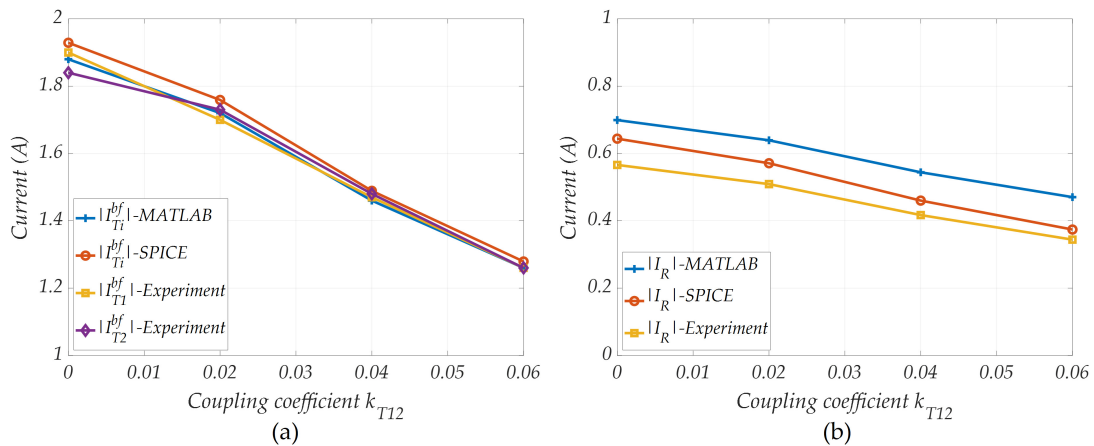
Figure 15. Current amplitude: (**a**) $|I_{Ti}^{bf}|$ and (**b**) $|I_R|$.

As shown in Figure 15, $|I_{Ti}^{bf}|$ and $|I_R|$ linearly decrease as k_{T12} increases from 0 to 0.06. These results are contrasted with the constant value of $|I_{Ti}^{bf}|$ and $|I_R|$ of Figure 11 when P_{in} is fixed. This difference is because the increase in k_{T12} generates the reactive power when the apparent power is fixed, which attenuates the active input power to the WPT system. This phenomenon is shown in the results of P_{in}, S_{in}, and Q_{in} of Figures 16a and 17a,b, respectively.

On the other hand, the MATLAB result of η_{MISO} shown in Figure 16c plots a different tendency compared to SPICE and experimental results. MATLAB result of η_{MISO} is constant at 24% regardless of k_{T12}, which is identical to the MATLAB result of η_{MISO} when P_{in} is fixed. It implies that the PTE is theoretically determined regardless of P_{in} or S_{in}. However, SPICE and experimental results in Figure 16c attenuate by about 5% as k_{T12} increases to 0.06, which is different from theoretical analysis. This η_{MISO} attenuation is mainly caused by a 0.65 V forward voltage drop of the diode used in a full-bridge rectifier. Because the two diodes in the rectifier conduct each cycle, an approximately 1.3 V voltage drop occurs. As shown in Figure 15b, $|I_R|$ decreases as k_{T12} increases which causes an induced voltage at the receiver to decrease. The greater η_{MISO} drop occurs as the induced voltage is lower since an attenuation rate of voltage increases due to the fixed voltage drop of the diode. In the worst case, no power is delivered to the load when the induced voltage is lower than the threshold voltage of the diode. For the above reasons, an increase in k_{T12} when the apparent power is fixed, η_{MISO} decreases in practice.

As shown in Figure 17, the results of S_{in}, Q_{in}, and PF_{in} show identical tendencies. As k_{T12} increases to 0.06 while S_{in} is supplied, Q_{in} increases to about 4 VA and P_{in} decreases to about 2.5 W. The decrease in P_{in} causes PF_{in} attenuation to about 0.5 as shown in Figure 17c.
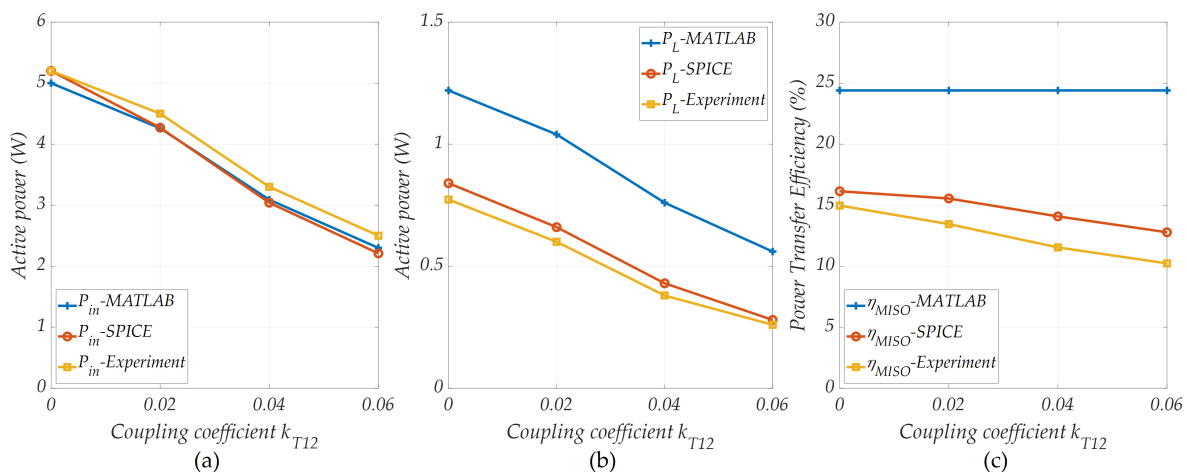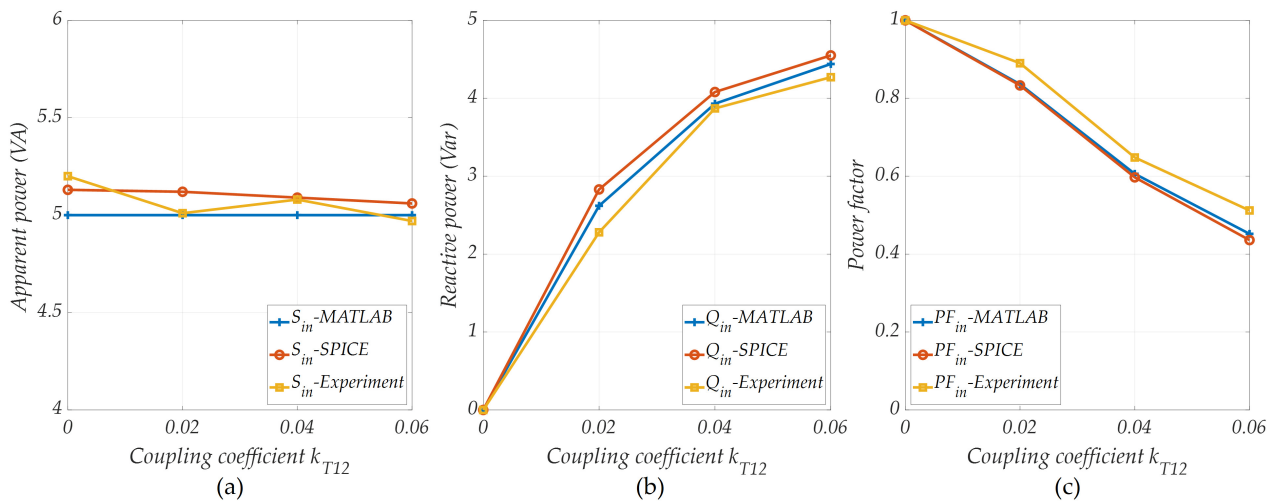

Figure 16. Results after applying $\overrightarrow{\mathbf{V_T^{bf}}}$: (**a**) P_{in}, (**b**) P_L, and (**c**) η_{MISO}.

Figure 17. Results after applying $\overrightarrow{\mathbf{V_T^{bf}}}$: (**a**) S_{in}, (**b**) Q_{in}, and (**c**) PF_{in}.

4.3. Discussion

Thus far, the influences caused by the intra-couplings in the transmitter array under magnetic beamforming have been verified from various viewpoints. All the MATLAB, SPICE, and experimental results match well. Based on the results, the advantages of magnetically independent transmitters have been derived when k_{T12} is 0 at all figures above: magnetic beamforming is achieved without adjusting the phase of the transmitter voltage, and the unity power factor is achieved by eliminating the reactive power. In addition, the maximum η_{MISO} is achieved when the transmitters are magnetically independent under the fixed S_{in}. This is because k_{T12} affects the PTE in this case due to the forward voltage drop of the diode.

4.3.1. Comparison to the State-of-the-Art in Terms of Power Factor Correction

The first advantage is that a simplified adjustment of $\overrightarrow{\mathbf{V_T^{bf}}}$ is intuitively confirmed in Section 3. From now on, we compare the second advantage of a unity power factor to other studies. Table 3 is a list of the power factor correction technology used in the recent WPT studies. Active PFC refers to correct the power factor by placing active devices such as a FET, while passive PFC refers to place passive elements for correction. As listed in Table 3, the setups in [30–37] are carried out under the SISO-WPT configuration using an active PFC rectifier or converter, which requires an additional DC power. The work in [38] uses LCL-topology in the SISO-WPT configuration to achieve a unity power factor for electric-vehicle charging. However, the work in [38] is limited to the SISO-WPT, and it is not known how LCL-topology is affected to the intra-couplings when the WPT is configured as multiple transmitters. The work in [23] uses the SIMO-WPT configuration and eliminates the intra-couplings in the receiver array by tuning resonance capacitance, which improves both power factor and power transfer efficiency. However, it also requires an additional power supply to adjust resonance capacitance. Compared to the above results, our analysis is the only result of how the intra-couplings of the transmitter in the MISO-WPT affect the power factor. Furthermore, it is confirmed that the power factor improves by simply adjusting the arrangement of the transmitter array without the deployment of passive or active elements.

Table 3. Existing WPT studies in terms of power factor correction.

Ref.	WPT Configuration	PFC Technique
[30–33]	SISO	Active—Front end rectifier
[34]	SISO	Active—Three phase rectifier
[35,36]	SISO	Active—Boost bridgeless rectifier
[37]	SISO	Active—Z-source converter
[38]	SISO	Passive—LCL toplology
[23]	SIMO	Active—Tuning resonance capacitance

4.3.2. Advantages of Magnetically Independent Transmitters for Real-Life Scenarios

Based on the equations derived in Sections 2 and 3, and the experimental results in Section 4, we draw specific advantages in terms of implementation to a real-life scenario: a MISO-WPT with magnetic beamforming for an electric vehicle (EV) charging. Figure 18 shows a concept of the MISO-WPT with magnetic beamforming for EV charging: (a) the fixed P_{in} at 300 W when k_T is 0.06, (b) the fixed P_{in} at 300 W when k_T is 0, and (c) the fixed S_{in} at 300 VA when k_T is 0.06. Other parameters are identical as in Table 2, except for P_{in} and S_{in}. The simulation results of $|\overrightarrow{\mathbf{V_T^{bf}}}|$, $\angle\overrightarrow{\mathbf{V_T^{bf}}}$, P_{in}, S_{in}, Q_{in}, and P_L are also denoted in Figure 18. As explained previously, the beamforming voltage $\overrightarrow{\mathbf{V_T^{bf}}}$ is calculated by Equation (20) when the intra-couplings of transmitter array occur and by Equation (22) when the intra-couplings are eliminated. Equations (20) and (22) of $\overrightarrow{\mathbf{V_T^{bf}}}$ are described as algorithms as shown in Figure 19a,b, respectively. These algorithms are executed at a microprocessor in the transmitter for magnetic beamforming, as shown in Figure 18.

As the algorithms should be continuously executed, the microprocessor is required at a certain level of performance. It is evident that the more complicated the algorithm, the higher the required microprocessor performance to be operated. In general, the efficiency of an algorithm is evaluated by its time complexity, and there are three types of time complexity: best, average, and worst case. Of the three types, the worst time complexity is expressed using "Big-O notation" that gives an upper bound on the resources required by an algorithm [39]. By analyzing both algorithms by Big-O notation, Figure 19a based on Equation (20) is $O(N^2)$ and Figure 19b based on Equation (22) is $O(N)$, where N is the number of transmitters. This indicates that as the number of transmitters increases, the time complexity of Equation (20) rapidly increases compared to Equation (22) when calculating $\overrightarrow{\mathbf{V_T^{bf}}}$. In other words, it indicates that the algorithm of Figure 19b can be implemented with a relatively low-power and low-performance microprocessor compared to the algorithm of Figure 19a. This is an advantage from a view of implementation cost when applying magnetically independent transmitters to the MISO-WPT with magnetic beamforming.

Other advantages are shown in Figure 18. Comparing Figure 18a,b when P_{in} is fixed at 300 W, $|\overrightarrow{\mathbf{V_T^{bf}}}|$ is varied as the intra-couplings k_{T12} varies. $|\overrightarrow{\mathbf{V_T^{bf}}}|$ is 45.5 V when k_{T12} is 0.06, while 20.6 V when k_{T12} is 0. In both cases, identical active power 73 W is transferred to the load. This result of increasing $|\overrightarrow{\mathbf{V_T^{bf}}}|$ when k_{T12} occurs is same when comparing Figure 18b,c when S_{in} is fixed at 300 VA: $|\overrightarrow{\mathbf{V_T^{bf}}}|$ is increased from 20.6 V to 30.6 V as k_{T12} increases. The results indicate that $|\overrightarrow{\mathbf{V_T^{bf}}}|$ should be increased in the presence of the intra-couplings when supplying the same apparent or active power. Furthermore, the difference in voltage amplitude increases as the input power increases (in our previous experiment, the voltage difference when P_{in} is fixed at 5 W is about 3 V, as shown in Figure 10a). This result indicates that a low-voltage operation is possible while supplying identical power when transmitters are magnetically independent. Owing to a low-voltage operation, it allows the designer to select elements or devices having a relatively low withstand voltage characteristic, thereby reducing the implementation cost.

In addition, an adjustment of $\angle\overrightarrow{\mathbf{V_T^{bf}}}$ is not required when transmitters are magnetically independent, as shown in Figure 18b. About 60 degrees of $\angle\overrightarrow{\mathbf{V_T^{bf}}}$ adjustment is required

when k_{T12} is 0.06, as shown in Figure 18a,c. Due to this characteristic, it is not necessary to deploy a phase shifter in each transmitter, which leads to reduce implementation costs.

In summary, the advantages of magnetically independent transmitters in terms of implementation costs are as follows: (1) using a low-cost microprocessor is possible due to a reduced computational complexity, (2) using elements and devices having a low withstand voltage is possible due to a low voltage operation, and (3) there is no necessary to deploy a phase shifter in each transmitter.
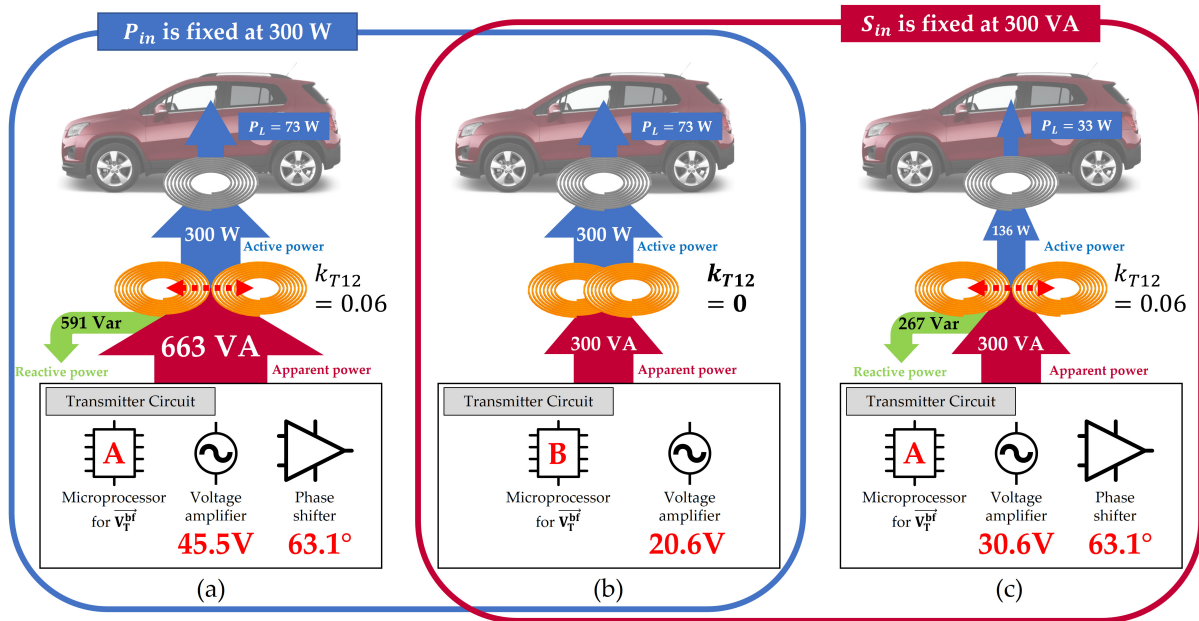

Figure 18. Concept of the MISO-WPT with magnetic beamforming for EV charging: (**a**) the fixed P_{in} at 300 W when k_T is 0.06; (**b**) the fixed P_{in} at 300 W when k_T is 0; and (**c**) the fixed S_{in} at 300 VA when k_T is 0.06.
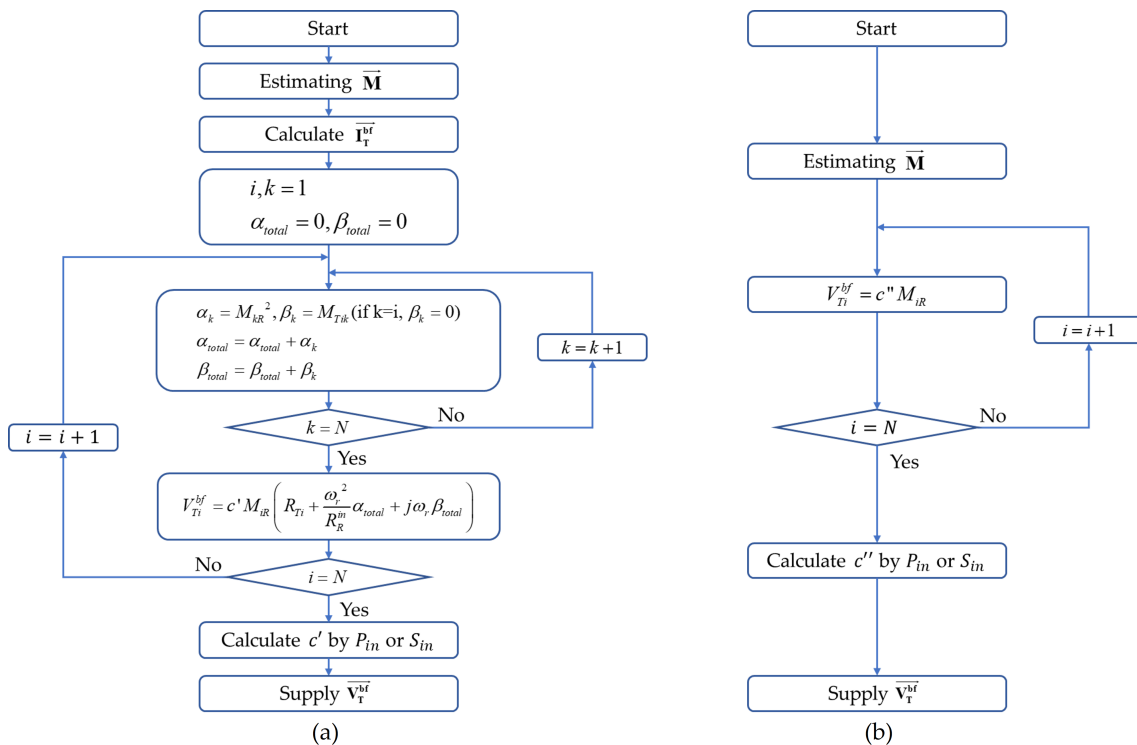

Figure 19. Algorithm for calculating $\overrightarrow{V_T^{bf}}$: (**a**) $\overrightarrow{V_T^{bf}}$ by Equation (20) and (**b**) $\overrightarrow{V_T^{bf}}$ by Equation (22).

5. Conclusions

This paper analyzes the influences caused by intra-couplings of the transmitter array in the MISO-WPT when applying magnetic beamforming. The theoretical analysis, MATLAB and SPICE simulation, and experiment are carried out under the conditions that the apparent power or active power is fixed at a specific value.

The influences caused by the intra-couplings are summarized as follows: (1) the intra-couplings cause amplitude and phase adjustment of a beamforming voltage, and (2) the intra-couplings cause power factor attenuation of each transmitter. Based on the analyses, the advantages when the transmitters become magnetically independent are derived: the magnetic beamforming is achieved by only adjusting the amplitude of transmitter voltage without phase adjustment, and the power factor becomes unity. These advantages are verified via SPICE simulation and experiment.

Our analysis provides a reason to consider the intra-couplings of transmitter array in the MISO-WPT. It contributes to simplifications of both the design and implementation procedures of a MISO-WPT applying magnetic beamforming. In addition, these results can be generalized for the MISO-WPT employing an arbitrary number of transmitters. It is expected that our analysis will play an essential role in the industries where WPT is essentially required, such as fields of the Internet of Things and electric vehicles. The efficient estimation of the magnetic channel, adaptive control of transmitters, and expansion of the MIMO-WPT are topics remaining for our future research.

Author Contributions: K.K. and H.-J.K. performed the theoretical analysis, simulation, experiment, and prepared the manuscript; D.-W.S. and J.-W.C. reviewed the paper and contributed the supervision. All authors have read and agreed to the published version of the manuscript.

Abbreviations

The following abbreviations are used in this manuscript:

WPT	Wireless Power Transfer
PTE	Power Transfer Efficiency
MIMO	Multiple-Inputs and Multiple-Outputs
MISO	Multiple-Inputs and Single-Output
PF	Power factor

Appendix A

In this Appendix, derivation of Equations (14) and (15) using linear algebra is introduced. Assume that there are two transmitters in the MISO-WPT. In this case, $\vec{\mathbf{H}}$ is a 2×2 matrix given by $\vec{\mathbf{H}} = [H_{1R}\ H_{2R}]$. Thus, $\vec{\mathbf{H}}^*\vec{\mathbf{H}}$ is

$$\vec{\mathbf{H}}^*\vec{\mathbf{H}} = \begin{bmatrix} H_{1R}{}^2 & H_{1R}H_{2R} \\ H_{1R}H_{2R} & H_{2R}{}^2 \end{bmatrix}. \tag{A1}$$

The eigenvalues λ and eigenvectors v of $\vec{\mathbf{H}}^*\vec{\mathbf{H}}$ are calculated using $det(\vec{\mathbf{H}}^*\vec{\mathbf{H}} - \lambda\mathbf{I}) = 0$, where $det(\mathbf{A})$ is a determinant of $N \times N$ matrix $\mathbf{A}$ and $\mathbf{I}$ is an identity matrix [40]. With this equation, the two eigenvalues are $\lambda_1 = 0$ and $\lambda_2 = H_{1R}{}^2 + H_{2R}{}^2$. The eigenvectors

corresponding to λ_1 and λ_2 are $v_1 \propto [-H_{2R} \ H_{1R}]^T$ and $v_2 \propto [H_{1R} \ H_{2R}]^T$. Thus, the largest real eigenvalue λ_{max} and v_{max} that corresponds to λ_{max} are given by

$$\lambda_{max} = H_{1R}{}^2 + H_{2R}{}^2, \tag{A2}$$

$$v_{max} \propto [H_{1R} \ H_{2R}]^T. \tag{A3}$$

Assuming the MISO-WPT has three transmitters, $\vec{\mathbf{H}}^* \vec{\mathbf{H}}$ is

$$\vec{\mathbf{H}}^* \vec{\mathbf{H}} = \begin{bmatrix} H_{1R}{}^2 & H_{1R}H_{2R} & H_{1R}H_{3R} \\ H_{1R}H_{2R} & H_{2R}{}^2 & H_{2R}H_{3R} \\ H_{1R}H_{3R} & H_{2R}H_{3R} & H_{3R}{}^2 \end{bmatrix}. \tag{A4}$$

Note that $\vec{\mathbf{H}}^* \vec{\mathbf{H}}$ has two eigenvalues of 0 and one eigenvalue $\lambda_3 = H_{1R}{}^2 + H_{2R}{}^2 + H_{3R}{}^2$. The eigenvector v_3 that corresponds to λ_3 is $v_3 \propto [H_{1R} \ H_{2R} \ H_{3R}]^T$. Thus, λ_{max} and v_{max} are given by

$$\lambda_{max} = H_{1R}{}^2 + H_{2R}{}^2 + H_{3R}{}^2, \tag{A5}$$

$$v_{max} \propto [H_{1R} \ H_{2R} \ H_{3R}]^T. \tag{A6}$$

To generalize λ_{max} and v_{max} for the MISO-WPT having arbitrary number of transmitters, assume that there are N transmitters deployed. $\vec{\mathbf{H}}^* \vec{\mathbf{H}}$ is

$$\vec{\mathbf{H}}^* \vec{\mathbf{H}} = \begin{bmatrix} H_{1R}{}^2 & H_{1R}H_{2R} & \cdots & H_{1R}H_{NR} \\ H_{1R}H_{2R} & H_{2R}{}^2 & \cdots & H_{2R}H_{NR} \\ \vdots & \vdots & \ddots & \vdots \\ H_{1R}H_{NR} & H_{2R}H_{NR} & \cdots & H_{NR}{}^2 \end{bmatrix}. \tag{A7}$$

The eigenvalues are $\lambda_1 = \lambda_2 = \cdots = \lambda_{N-1} = 0$, and $\lambda_N = H_{1R}{}^2 + H_{2R}{}^2 + \cdots + H_{NR}{}^2$. The eigenvector v_N that corresponds to λ_N is $v_N \propto [H_{1R} \ H_{2R} \ \cdots \ H_{NR}]^T$, which is summarized as

$$\lambda_{max} = H_{1R}{}^2 + H_{2R}{}^2 + \cdots + H_{NR}{}^2 = \sum_{i=1}^{N} H_{iR}{}^2, \tag{A8}$$

$$v_{max} \propto [H_{1R} \ H_{2R} \ \cdots \ H_{NR}]^T \propto \vec{\mathbf{H}}^T. \tag{A9}$$

As $\vec{\mathbf{H}}$ is proportional to $\vec{\mathbf{M}}^T$ by Table 1, v_{max} of Equation (A9) is determined by a function of $\vec{\mathbf{M}}^T$, thus

$$v_{max} = d\,\vec{\mathbf{M}}^T, \tag{A10}$$

where d is a constant for normalizing v_{max} to a unit vector.

References

1. Mou, X.; Groling, O.; Sun, H. Energy-efficient and adaptive design for wireless power transfer in electric vehicles. *IEEE Trans. Ind. Electron.* **2017**, *64*, 7250–7260. [CrossRef]
2. Lu, F.; Zhang, H.; Hofmann, H.; Mi, C.C. A dynamic charging system with reduced output power pulsation for electric vehicles. *IEEE Trans. Ind. Electron.* **2016**, *63*, 6580–6590. [CrossRef]
3. Sampath, J.; Vilathgamuwa, D.M.; Alphones, A. Efficiency enhancement for dynamic wireless power transfer system with segmented transmitter array. *IEEE Trans. Transp. Electrif.* **2015**, *2*, 76–85. [CrossRef]
4. Sun, L.; Ma, D.; Tang, H. A review of recent trends in wireless power transfer technology and its applications in electric vehicle wireless charging. *Renew. Sustain. Energy Rev.* **2018**, *91*, 490–503. [CrossRef]
5. Hajiaghajani, A.; Ahn, S. Single-sided near-field wireless power transfer by a three-dimensional coil array. *Micromachines* **2019**, *10*, 200. [CrossRef]
6. Xu, Q.; Wang, H.; Gao, Z.; Mao, Z.H.; He, J.; Sun, M. A novel mat-based system for position-varying wireless power transfer to biomedical implants. *IEEE Trans. Magn.* **2013**, *49*, 4774–4779. [CrossRef]
7. Vamvakas, P.; Tsiropoulou, E.E.; Vomvas, M.; Papavassiliou, S. Adaptive power management in wireless powered communication networks: A user-centric approach. In Proceedings of the 2017 IEEE 38th Sarnoff Symposium, Newark, NJ, USA, 18–20 September 2017; pp. 1–6.

8. Campi, T.; Cruciani, S.; Feliziani, M. Wireless power transfer technology applied to an autonomous electric UAV with a small secondary coil. *Energies* **2018**, *11*, 352. [CrossRef]

9. Lu, X.; Wang, P.; Niyato, D.; Kim, D.I.; Han, Z. Wireless charging technologies: Fundamentals, standards, and network applications. *IEEE Commun. Surv. Tutor.* **2015**, *18*, 1413–1452. [CrossRef]

10. Kurs, A.; Karalis, A.; Moffatt, R.; Joannopoulos, J.D.; Fisher, P.; Soljačić, M. Wireless power transfer via strongly coupled magnetic resonances. *Science* **2007**, *317*, 83–86. [CrossRef]

11. Masihpour, M.; Agbinya, J.I. Cooperative relay in Near Field Magnetic Induction: A new technology for embedded medical communication systems. In Proceedings of the 2010 Fifth International Conference on Broadband and Biomedical Communications, Malaga, Spain, 15–17 December 2010; pp. 1–6.

12. Park, C.; Lee, S.; Cho, G.H.; Rim, C.T. Innovative 5-m-off-distance inductive power transfer systems with optimally shaped dipole coils. *IEEE Trans. Power Electron.* **2014**, *30*, 817–827. [CrossRef]

13. Miwa, K.; Mori, H.; Kikuma, N.; Hirayama, H.; Sakakibara, K. A consideration of efficiency improvement of transmitting coil array in wireless power transfer with magnetically coupled resonance. In Proceedings of the 2013 IEEE Wireless Power Transfer (WPT), Perugia, Italy, 15–16 May 2013; pp. 13–16.

14. Jadidian, J.; Katabi, D. Magnetic MIMO: How to charge your phone in your pocket. In Proceedings of the 20th Annual International Conference on Mobile Computing and Networking, Maui, HI, USA, 7–11 September 2014; pp. 495–506.

15. Shi, L.; Kabelac, Z.; Katabi, D.; Perreault, D. Wireless power hotspot that charges all of your devices. In Proceedings of the 21st Annual International Conference on Mobile Computing and Networking, New Orleans, LA, USA, 25–29 October 2015; pp. 2–13.

16. Waters, B.H.; Mahoney, B.J.; Ranganathan, V.; Smith, J.R. Power delivery and leakage field control using an adaptive phased array wireless power system. *IEEE Trans. Power Electron.* **2015**, *30*, 6298–6309. [CrossRef]

17. Oodachi, N.; Ogawa, K.; Kudo, H.; Shoki, H.; Obayashi, S.; Morooka, T. Efficiency improvement of wireless power transfer via magnetic resonance using transmission coil array. In Proceedings of the 2011 IEEE International Symposium on Antennas and Propagation (APSURSI), Atlanta, GA, USA, 7–12 July 2011; pp. 1707–1710.

18. Kisseleff, S.; Akyildiz, I.F.; Gerstacker, W. Beamforming for magnetic induction based wireless power transfer systems with multiple receivers. In Proceedings of the 2015 IEEE Global Communications Conference (GLOBECOM), San Diego, CA, USA, 6–10 December 2015; pp. 1–7.

19. Kim, H.J.; Park, J.; Oh, K.S.; Choi, J.P.; Jang, J.E.; Choi, J.W. Near-field magnetic induction MIMO communication using heterogeneous multipole loop antenna array for higher data rate transmission. *IEEE Trans. Antennas Propag.* **2016**, *64*, 1952–1962. [CrossRef]

20. Yoo, S.S.; Lee, K.Y.; Yoo, H.J. Coupling-Shielded Inductor for High Isolation Between PA and LC-Based DCO. *IEEE Electron Device Lett.* **2016**, *38*, 24–27. [CrossRef]

21. Tang, S.; Hui, S.; Chung, H.H. Evaluation of the shielding effects on printed-circuit-board transformers using ferrite plates and copper sheets. *IEEE Trans. Power Electron.* **2002**, *17*, 1080–1088. [CrossRef]

22. Tal, N.; Morag, Y.; Levron, Y. Magnetic induction antenna arrays for MIMO and multiple-frequency communication systems. *Prog. Electromagn. Res.* **2017**, *75*, 155–167. [CrossRef]

23. Fu, M.; Zhang, T.; Zhu, X.; Luk, P.C.K.; Ma, C. Compensation of cross coupling in multiple-receiver wireless power transfer systems. *IEEE Trans. Ind. Inform.* **2016**, *12*, 474–482. [CrossRef]

24. Pantic, Z.; Bai, S.; Lukic, S.M. ZCS *LCC*-compensated resonant inverter for inductive-power-transfer application. *IEEE Trans. Ind. Electron.* **2010**, *58*, 3500–3510. [CrossRef]

25. Sohn, Y.H.; Choi, B.H.; Lee, E.S.; Lim, G.C.; Cho, G.H.; Rim, C.T. General unified analyses of two-capacitor inductive power transfer systems: Equivalence of current-source SS and SP compensations. *IEEE Trans. Power Electron.* **2015**, *30*, 6030–6045. [CrossRef]

26. Wang, C.S.; Stielau, O.H.; Covic, G.A. Design considerations for a contactless electric vehicle battery charger. *IEEE Trans. Ind. Electron.* **2005**, *52*, 1308–1314. [CrossRef]

27. Alexander, C.K.; Sadiku, M.N.O. *Fundamentals of Electric Circuits*; McGraw-Hill: New York, NY, USA, 2017; Volume 6.

28. Glover, J.D.; Sarma, M.S.; Overbye, T. *Power System Analysis & Design, SI Version*; Cengage Learning: Boston, MA, USA, 2012.

29. Florian, C.; Mastri, F.; Paganelli, R.P.; Masotti, D.; Costanzo, A. Theoretical and numerical design of a wireless power transmission link with GaN-based transmitter and adaptive receiver. *IEEE Trans. Microw. Theory Tech.* **2014**, *62*, 931–946. [CrossRef]

30. Tang, L.; Chinthavali, M.; Onar, O.C.; Campbell, S.; Miller, J.M. SiC MOSFET based single phase active boost rectifier with power factor correction for wireless power transfer applications. In Proceedings of the 2014 IEEE Applied Power Electronics Conference and Exposition-APEC, Fort Worth, TX, USA, 16–20 March 2014; pp. 1669–1675.

31. Chinthavali, M.S.; Onar, O.C.; Miller, J.M.; Tang, L. Single-phase active boost rectifier with power factor correction for wireless power transfer applications. In Proceedings of the 2013 IEEE Energy Conversion Congress and Exposition, Denver, CO, USA, 15–19 September 2013; pp. 3258–3265.

32. Kiratipongvoot, S.; Yang, Z.; Lee, C.K.; Ho, S.S. Design a high-frequency-fed unity power-factor AC-DC power converter for wireless power transfer application. In Proceedings of the 2015 IEEE Energy Conversion Congress and Exposition (ECCE), Montreal, QC, Canada, 20–24 September 2015; pp. 599–606.

33. Pickelsimer, M.; Tolbert, L.; Ozpineci, B.; Miller, J.M. Simulation of a wireless power transfer system for electric vehicles with power factor correction. In Proceedings of the 2012 IEEE International Electric Vehicle Conference, Greenville, SC, USA, 4–8 March 2012; pp. 1–6.
34. Liu, J.; Xu, W.; Chan, K.W.; Liu, M.; Zhang, X.; Chan, N.H.L. A three-phase single-stage AC–DC wireless-power-transfer converter with power factor correction and bus voltage control. *IEEE J. Emerg. Sel. Top. Power Electron.* **2019**, *8*, 1782–1800. [CrossRef]
35. Liu, J.; Chan, K.W.; Chung, C.Y.; Chan, N.H.L.; Liu, M.; Xu, W. Single-stage wireless-power-transfer resonant converter with boost bridgeless power-factor-correction rectifier. *IEEE Trans. Ind. Electron.* **2017**, *65*, 2145–2155. [CrossRef]
36. González-Santini, N.S.; Zeng, H.; Yu, Y.; Peng, F.Z. Z-source resonant converter with power factor correction for wireless power transfer applications. *IEEE Trans. Power Electron.* **2016**, *31*, 7691–7700. [CrossRef]
37. Hsieh, Y.C.; Lin, Z.R.; Chen, M.C.; Hsieh, H.C.; Liu, Y.C.; Chiu, H.J. High-efficiency wireless power transfer system for electric vehicle applications. *IEEE Trans. Circuits Syst. II Express Briefs* **2016**, *64*, 942–946. [CrossRef]
38. Park, M.; Yu, S.D.; Yim, S.W.; Park, K.; Min, B.D.; Kim, S.D.; Cho, J.G. A study of wireless power transfer topologies for 3.3 kW and 6.6 kW electric vehicle charging infrastructure. In Proceedings of the 2016 IEEE Transportation Electrification Conference and Expo, Asia-Pacific (ITEC Asia-Pacific), Busan, Korea, 1–4 June 2016; pp. 689–692.
39. Chivers, I.; Sleightholme, J. An introduction to Algorithms and the Big O Notation. In *Introduction to Programming with Fortran*; Springer: Berlin/Heidelberg, Germany, 2015; pp. 359–364.
40. Strang, G. *Introduction to Linear Algebra*; Cambridge Press: Wellesley, MA, USA, 1993; Volume 3.